

# An Overabundance of Black Hole X-Ray Binaries in the Galactic Center from Tidal Captures

A. Generozov<sup>\*</sup>, N. C. Stone<sup>1</sup>, B. D. Metzger, J. P. Ostriker

*Columbia Astrophysics Laboratory, Pupin Hall, Columbia University, 550 W. 120th Street, New York, NY 10027, USA*

<sup>1</sup>*Einstein Fellow*

6 April 2018

## ABSTRACT

A large population of X-ray binaries (XRBs) was recently discovered within the central parsec of the Galaxy by Hailey et al. (2018). While the presence of compact objects on this scale due to radial mass segregation is, in itself, unsurprising, the fraction of *binaries* would naively be expected to be small because of how easily primordial binaries are dissociated in the dynamically hot environment of the nuclear star cluster (NSC). We propose that the formation of XRBs in the central parsec is dominated by the *tidal capture* of stars by black holes (BHs) and neutron stars (NSs). We model the time-dependent radial density profiles of stars and compact objects in the NSC with a Fokker-Planck approach, using the present-day stellar population and rate of *in situ* massive star (and thus compact object) formation as observational constraints. Of the  $\sim 1 - 4 \times 10^4$  BHs that accumulate in the central parsec over the age of the Galaxy, we predict that  $\sim 60 - 200$  currently exist as BH-XRBs formed from tidal capture, consistent with the population seen by Hailey et al. (2018). A somewhat lower number of tidal capture NS-XRBs is also predicted. We also use our observationally calibrated models for the NSC to predict rates of other exotic dynamical processes, such as the tidal disruption of stars by the central supermassive black hole ( $\sim 10^{-4}$  per year at  $z=0$ ).

**Key words:** black holes physics

## 1 INTRODUCTION

A large fraction of low- to moderate-mass galaxies host nuclear star clusters (NSCs). The large mean stellar densities in these clusters, typically  $\sim 10^2 - 10^6 M_{\odot} \text{ pc}^{-3}$  (e.g. Georgiev & Böker 2014), result in correspondingly high rates of collisional interactions (Leigh et al. 2016). Stellar-mass compact objects, particularly black holes (BHs) and neutron stars (NSs), play an important role in these environments; for example, they form sources of *LIGO* and *LISA*-band gravitational wave (e.g. Quinlan & Shapiro 1987; O’Leary et al. 2009; Tsang 2013; Bar-Or & Alexander 2016; Antonini & Rasio 2016; Stone et al. 2017a; Bartos et al. 2017), serve as probes of the relativistic spacetime near the central supermassive BH (SMBH; Paczynski & Trimble 1979; Pfahl & Loeb 2004), and potentially contribute to the  $\gamma$ -ray excess observed in our own Galactic Center (GC; Brandt & Kocsis 2015). Compact objects in NSCs will also induce strong tidal interactions during close flybys with stars. A sequence of weak tidal encounters will stochastically spin up GC stars (Alexander & Kumar 2001; Sazonov et al. 2012), while a sin-

gle very strong tidal encounter may disrupt the victim star and produce a luminous transient (Perets et al. 2016), but a tidal encounter of intermediate strength will bind the star to the compact object in a “tidal capture” (Fabian et al. 1975), as is the focus of this paper.

There is strong evidence of a population of NSs and stellar-mass BHs in the Milky Way (MW) GC. The hundreds of O/B stars currently located in the central parsec indicate a high rate of *in situ* NS/BH formation in this region (e.g. Levin & Beloborodov 2003; Genzel et al. 2003). The discovery of even a single magnetar within  $\lesssim 0.1$  pc of Sgr A\* (Mori et al. 2013), given their short active lifetimes, also demands a high current rate of NS formation. The X-ray point sources in the GC also directly indicate a population of *binaries* containing compact objects. There are a total of six known X-ray transients in the central parsec (Muno et al. 2005; Hailey & Mori 2017). Of these six, three are strong BH X-ray binary (BH-XRB) candidates based on their spectral properties and the long time-scale ( $> 10$  years) between their outbursts. The identity of the remaining transients is unknown, but they may be NS-XRBs. As NS-XRBs have large outbursts every 5–10 years, any that are present in the GC would have been seen by the *Swift* satellite’s XRT, im-

\* ag@astro.columbia.edu

plying that there are at most three in the central parsec (Hailey et al. 2018). In addition to these transient sources, Hailey et al. (2018) recently discovered six candidate quiescent BH-XRBs concentrated within the central parsec; they also identify six ambiguous sources, which could be either BH-XRBs or millisecond pulsars (MSPs). Reasonable extrapolation of the point source luminosity function below the instrumental detection threshold implies a true number of BH-XRBs inside the central parsec in the hundreds.

The number of BH-XRBs in the GC per unit stellar mass exceeds that of the field population by a factor of  $\gtrsim 100 - 1000$  (Table 1). This suggests that the unusual environment of the GC dynamically - and efficiently - assembles BH-XRBs, in a manner analogous to the dynamical overproduction of NS-XRBs in globular clusters (Katz 1975; Benacquista & Downing 2013). Although a high concentration of compact objects in the GC is itself unsurprising (Alexander & Hopman 2009), an overabundance of mass-transferring binaries is more challenging to understand. In other dense stellar systems like globular clusters, exchange interactions that swap compact objects into binaries can explain the overabundance of NS-XRBs and their MSP progeny (e.g. Ivanova et al. 2008). However, this channel is strongly suppressed in NSCs because nearly all primordial stellar binaries would be evaporated by three-body encounters, and those that survive would be so hard as to present a minimal cross-section for exchange interactions (see Leigh et al. 2017 and appendix C).<sup>1</sup>

This paper instead focuses on an alternative channel of XRB formation: the tidal capture of main sequence stars by compact objects (Press & Teukolsky 1977; Lee & Ostriker 1986). Stars which pass sufficiently close to a compact object - approximately, within its tidal radius  $r_t$  - are completely torn apart by tidal forces (e.g. Rees 1988). However, for pericenter radii somewhat larger than  $r_t$ , tidal forces are not necessarily destructive; instead, they transfer orbital energy into internal oscillations of the star, binding it to the compact object. Following a complex and potentially violent process of circularization, the newly-created binary settles into a tight orbit. The necessarily small orbital separation of the tidal capture binary guarantees that subsequent gravitational wave emission will drive the star into Roche Lobe overflow in less than a Hubble time, forming a mass-transferring X-ray source. The high density of compact objects and stars in the GC inevitably lead to a significant rate of tidal captures, representing a promising explanation for the observed overabundance of BH- and NS-XRBs.

This paper is organized as follows. In § 2 we describe our model for the dynamical evolution of stars and compact remnants in the GC. In § 3 we use the time-dependent density profiles of the stars and compact objects from our NSC models to calculate the rates of collisions and tidal capture of stars by compact objects, and make predictions for the present-day BH and NS-XRB population. In § 4 we compare our predictions to observations of the XRB populations in the GC measured by Hailey et al. (2018). In § 5 we describe

several auxiliary predictions of our model for the rates of stellar interactions and exotic transients. In § 6 we briefly summarize our results and conclude.

## 2 GALACTIC NSC MODEL

The number of BH-XRBs which form in the GC clearly depends on the number of stellar-mass BHs that reside there. Previous works have predicted that  $\gtrsim 10^3 - 10^4$  BHs accumulate within the central parsec over timescales of several Gyr due to radial mass segregation from the stellar population on larger scales (e.g. Morris 1993; Miralda-Escudé & Gould 2000; Freitag et al. 2006; Hopman & Alexander 2006b; O’Leary et al. 2009; Dale et al. 2009; Merritt 2010). Most previous models assume that the BHs are distributed at birth in the same way as the lower mass stars, and neglect ongoing star formation (though see Aharon & Perets 2015; Baumgardt et al. 2017).

In fact, much of our NSC’s total stellar population was likely deposited by the infall of globular clusters early in its history (Tremaine et al. 1975; Gnedin et al. 2014). Historically, globular clusters (at least of the kind which survive to the present day) were predicted to lose all but a few of their BHs due to strong kicks in multi-body interactions during a core collapse or Spitzer instability phase (e.g. Spitzer 1987; Kulkarni et al. 1993; Banerjee et al. 2010). Such lossiness would limit the ability of globular infall to seed the GC with BHs, although Morscher et al. (2015) challenged this conventional wisdom by showing that  $\sim 10^2 - 10^3$  BHs could be retained in globulars due to three-body processes reversing core collapse.<sup>2</sup> While a few candidate globular cluster BH-XRB have been identified (Strader et al. 2012b; Bahramian et al. 2017) in the MW, and other BH-XRBs have been seen in extragalactic globulars (Maccarone et al. 2007), the total inventory of globular BHs is challenging to infer from observations because the number of BH-XRBs is likely a weak function of the number of retained BHs (Kremer et al. 2017).

A potentially much larger population of BHs is formed in the GC by *in situ* star formation. A disk of young stars of age  $\approx 4$  Myr is observed to extend between  $\sim 0.03 - 0.3$  pc of SgrA\* (Krabbe et al. 1995; Paumard et al. 2006; Lu et al. 2013), containing a total of  $\sim 100$  WR/O stars with a top-heavy initial mass function (IMF; e.g. Bartko et al. 2010; Lu et al. 2013). If star formation episodes similar to those responsible for the observed disks occur regularly every  $\sim 10 - 100$  Myr, then a total of  $\sim 10^4 - 10^5$  NSs and BHs were injected into the central parsec over the last  $\sim 10$  Gyr since its formation. This source of massive compact objects likely dominates over mass segregation from larger scales, and over primordial globular cluster infall.

This section describes our model for how the 1D radial density profiles of stars and compact remnants in the GC evolve in time. Our goal is to create a small set of simple but physically-motivated models for building up the NSC, which are consistent with both the present-day stellar density profile and the observed rate of compact object formation. Motivated by the above discussion, our model consists

<sup>1</sup> Note that the maximum semi-major axis above which binaries are evaporated scales as velocity dispersion  $\sigma^{-2}$ , whereas the maximum pericenter for tidal capture scales  $\sigma^{-0.2}$ ; see appendix C for more details.

<sup>2</sup> Physically, this is because the thermodynamics of the subcluster is regulated by the longer relaxation time of the bulk cluster (Breen & Heggie 2012, 2013).

**Table 1.** Estimated abundances of NS-XRB/BH-XRB/MSP per unit stellar mass in different environments. *NS-XRBs*: The Milky Way contains  $\sim 100$  identified field NS-XRBs. Galactic globular clusters contain 15 (transiently or persistently) bright NS-XRBs, but only  $\sim 0.1\%$  of the Galaxy’s stellar mass (Benacquista & Downing 2013). Furthermore, NS-XRBs are concentrated in dense, massive clusters with high encounter rates like Terzan 5 (Verbunt & Hut 1987; Heinke et al. 2003; Pooley & Hut 2006). The central parsec of the GC contains  $\sim 1-3$  NS-XRBs (Degenaar et al. 2012; Hailey et al. 2018) and  $\sim 10^6 M_\odot$  in stars. *BH-XRBs*: Observed BH transients in the field suggest a galactic population of 1000 BH-XRB (Corral-Santana et al. 2016) (assuming that outbursts occur on average every  $\sim 100$  years). Three candidate BH X-ray transients were detected in the central parsec by *Chandra* and *Swift* over 15 years (Muno et al. 2005; Hailey & Mori 2017). This suggests a total of  $\sim 20$  BH X-ray transients in this volume. In addition Hailey et al. (2018) a population of 6-12 *quiescent* BH XRB candidates in this region (with possibly hundreds below the detection threshold). Other studies have identified 4 quiescent BH XRB candidates in Galactic globular clusters (Strader et al. 2012a,b; Miller-Jones et al. 2015; Bahramian et al. 2017). No outbursts have been seen from globular BH XRB candidates, while only one quiescent BH XRB candidate has been identified in the field (Tetarenko et al. 2016). *MSPs*: A total of 266 MSPs are observed in the field, while 133 MSPs are observed in globular clusters. Up to  $\sim 200$  MSPs could reside in the central parsec (Perez et al. 2015).

Environment	$N_{\text{NS-XRB}} \text{ (B)}$ [ $M_\odot^{-1}$ ]	$N_{\text{NS-XRB}} \text{ (Q)}$ [ $M_\odot^{-1}$ ]	$N_{\text{BH-XRB}} \text{ (T)}$ [ $M_\odot^{-1}$ ]	$N_{\text{BH-XRB}} \text{ (Q)}$ [ $M_\odot^{-1}$ ]	$N_{\text{MSP}}$	References
Field	$2 \times 10^{-9}$	–	$2 \times 10^{-8}$	–	$5 \times 10^{-9}$	1-3
Globular clusters (all)	$3 \times 10^{-7}$	$6 \times 10^{-7}$	–	$10^{-7}$	$7 \times 10^{-6}$	5-7
47 Tuc	–	$7 \times 10^{-6}$	–	$10^{-6}$	$3 \times 10^{-5}$	8-11
Terzan 5	$1.5 \times 10^{-6}$	$6 \times 10^{-6}$	–	–	$2 \times 10^{-5}$	12-13
Galactic Center (central parsec)	$1-3 \times 10^{-6}$	–	$2 \times 10^{-5}$	$10^{-5}$	$\lesssim 1.3 \times 10^{-4}$	14-18

**Notes** Q=Quiescent LMXBs ( $L_x \lesssim 10^{33}$  erg s $^{-1}$ ); T=Transient LMXBs; B=Persistently bright or transient LMXBs (only persistently bright sources are NSs)

**References** (1) Corral-Santana et al. (2016) (2) Tetarenko et al. (2016) (3) Galactic MSPs (4) Benacquista & Downing (2013) (5) Strader et al. (2012a) (6) Strader et al. (2012b) (7) Globular MSPs (8) Miller-Jones et al. (2015) (9) Bahramian et al. (2017) (10) Heinke et al. (2005b) (11) Heinke et al. (2005a) (12) Heinke et al. (2006) (13) Bahramian et al. (2014) (14) Degenaar et al. (2015) (15) Muno et al. (2005) (16) Hailey & Mori (2017) (17) Hailey et al. (2018) (18) Perez et al. (2015)

of two stellar populations: (1) stars injected in the distant past, near the formation time of the NSC; and (2) a continuously forming *in-situ* population with a top heavy IMF concentrated within the central parsec, as is motivated by the observed disks of young stars (Lu et al. 2013). All of our models assume spherical symmetry and isotropic velocities.

In §2.1 we motivate the parameters of our models using the observed stellar populations and constraints on the star formation history in the GC. In §2.2 we describe our numerical procedure for evolving the density profiles of stars and compact objects through two-body relaxation. To build up physical intuition, we first calculate how the compact objects evolve in isolation in §2.3, before adding the effects of the stellar background in §2.4. In §2.5 we discuss several additional hypothetical scenarios for building the NSC, in order to assess the range of uncertainties in our work and to make contact with previous work on this topic in the literature (which generally neglect centrally-concentrated compact object formation).

## 2.1 Stellar and Compact Object Populations

Eighty percent of the stars in the GC are older than 5 Gyr (Pfuhl et al. 2011), consistent with the bulk of the NSC’s growth being due to the infall of globular clusters via dynamical friction over a period of  $\sim 1$  Gyr in the early history of the Galaxy (Gnedin et al. 2014). The observed diffuse stellar light<sup>3</sup> is well fit by the parameterization (Schödel et al.

2018; their Tables 2 and 3),

$$\rho_*(r) = 2^{(\beta-\gamma)/\alpha} \rho_0 \left(\frac{r}{r_0}\right)^{-\gamma} \left(1 + \left(\frac{r}{r_0}\right)^\alpha\right)^{(\gamma-\beta)/\alpha}, \quad (1)$$

with best-fit parameters of  $\gamma = 1.16 \pm 0.02$ ,  $\beta = 3.2 \pm 0.3$ ,  $r_0 = 3.2 \pm 0.2$  pc for fixed  $\alpha = 10$ . The density normalization at 1 pc is  $0.8 - 1.7 \times 10^5$  pc $^{-3}$ .<sup>4</sup>

Compact objects are also deposited at early times if they arrive with the globular clusters. Ivanova et al. (2008) estimate that a typical globular cluster retains 1 NS per  $10^3 M_\odot$  of other stars. Although globulars may also bring in a sizeable BH population, this is less certain because, as discussed above, BHs may be ejected from globulars by binary-single interactions (e.g. Kulkarni et al. 1993; Banerjee et al. 2010; see, however, Morscher et al. 2015). Given this uncertainty, and because the current BH population is anyways likely to be dominated by *in situ* star formation (see below), we neglect BHs deposited with the old stellar population.

Our fiducial models include a population of compact objects formed *in situ*, motivated by the sub-parsec disk of young stars observed in the GC. The K-band luminosity function of the young stars is consistent with a single starburst that occurred 2.5–5.8 Myr ago (Lu et al. 2013; Habibi et al. 2017). The burst produced a total of  $\sim 250$  stars of mass  $\gtrsim 8 M_\odot$  with an IMF of the form  $dN/dm \propto m^{-\beta}$  with  $\beta \approx 1.7$ . If stars with masses in the range  $m \approx 8 - 25 M_\odot$  form NSs, while those with  $m \gtrsim 25 M_\odot$  form BHs, then a

<sup>3</sup> This profile differs from the observed giant density profile, which has a core inside of  $\sim 0.5$  pc (the so-called “missing giants” problem; e.g. Buchholz et al. 2009; Do et al. 2009). The diffuse light tracks emission from early G and late F main sequence and sub-giant stars, and is likely a better probe of the underlying stellar density. One solution to the missing giants problem is

mass-stripping by collisions between the giants with other stars and compact objects (Dale et al. 2009) or with a clumpy gas disc (Amaro-Seoane & Chen 2014; Kieffer & Bogdanović 2016).

<sup>4</sup> We use the values from the first preprint version of Schödel et al. (2018). The best fit parameters are slightly different in the published version, but consistent within uncertainties.

total of  $N_{\text{ns}} \sim 160$  NSs and  $N_{\text{bh}} \sim 90$  BHs were, or will be, formed from the disk stars. If the time since the last star formation episode of  $\approx 4$  Myr is comparable to the typical interval between starbursts, then the implied average formation rates of NSs and BHs in the central parsec are  $\dot{N}_{\text{ns}} \sim 4 \times 10^{-5} \text{ yr}^{-1}$  and  $\dot{N}_{\text{bh}} \sim 2 \times 10^{-5} \text{ yr}^{-1}$ , respectively.

The above estimates assume that the current epoch is a representative snapshot of the central parsec’s average star formation history. In possible tension with this, [Pfuhl et al. \(2011\)](#) find that the star formation rate  $\sim 1 - 5$  Gyr ago was  $\sim 1 - 2$  orders magnitude smaller than the present-day rate (their Figure 14), in which case the average star formation rate is  $\lesssim 10\%$  of its recent value. However these observations probe only low mass stars ( $\lesssim 2M_{\odot}$ ), and thus do not constrain the rate of NS/BH formation within the star-forming disks if the top-heavy disk IMF is truncated below a few solar masses. Other nearby galactic nuclei such as M31 possess disks of A stars, but no O and B stars ([Leigh et al. 2016](#)); in these NSCs at least, the last major episode of star formation occurred  $\gtrsim 100$  Myr ago.

Motivated by the above, we construct our fiducial models for the GC using the following three populations:

- “Primordial” stars, which are assumed to form impulsively at  $t = 0$  (10 Gyr ago) with an initial density profile following eq. (1). We model all the stars as being of a single mass  $0.3M_{\odot}$ , which represents the root-mean-square mass of the main sequence in an evolved Kroupa IMF. The parameters of the stellar profile  $(\alpha, \beta, \gamma)$  are fixed to the best-fit values from [Schödel et al. \(2018\)](#), except for the scale radius  $r_o$  and normalization  $\rho_o$ . The cluster expands radially over time, so we chose smaller initial values of  $r_o = 0.5, 1.5$  pc than the current best-fit value in order to match the *present-day* stellar density profile (for which  $r_o \approx 3$  pc). A normalization of  $\rho_{\star}(1 \text{ pc}) = 1.1 \times 10^5 M_{\odot} \text{ pc}^{-3}$  is chosen to fix the total stellar mass at a value of  $5.7 \times 10^7 M_{\odot}$ .<sup>5</sup>
- “Primordial” NSs of mass  $1.5M_{\odot}$ , which are deposited impulsively at  $t = 0$  with the same density profile as the stars. The total number of NSs is normalized to a fraction  $10^{-3}$  of the number of stars, motivated by their expected abundance in globular clusters ([Ivanova et al. 2008](#)).
- Compact objects from *in situ* star formation (NSs and BHs of masses  $1.5$  and  $10M_{\odot}$ , respectively) that are continuously injected near the present-day disk of young stars. The source term is narrowly peaked at the potential energy at  $0.3$  pc (the outer edge of the disk). In physical space, star formation is concentrated inside of this radius with an  $r^{-0.5}$  density profile. We found our results do not change if the star formation is instead concentrated inside of  $0.03$  pc (the inner edge of the star forming disks). In our “**Fiducial**” model, we adopt conservative formation rates of  $\dot{N}_{\text{ns}} = 4 \times 10^{-6} \text{ yr}^{-1}$  and  $\dot{N}_{\text{bh}} = 2 \times 10^{-6} \text{ yr}^{-1}$ , respectively. We also consider a model (“**Fiducial**  $\times 10$ ”) in which  $\dot{N}_{\text{ns}}$  and  $\dot{N}_{\text{bh}}$  are ten times larger, corresponding to the present day formation rate of massive stars.

<sup>5</sup> This is the total mass assuming the density profile extends to infinity; in reality the profile steepens outside of  $\sim 10$  pc, such that the true total mass  $2.5 \pm 0.4 \times 10^7 M_{\odot}$  is somewhat lower.

The parameters of our fiducial models are summarized in Table 2. Several hypothetical (non-fiducial) models are introduced in §2.5 in order to assess the robustness of our conclusions.

## 2.2 Numerical Method: Fokker-Planck

The radial distribution of stars and compact objects evolves over time due to two-body relaxation. We follow this evolution using the PHASEFLOW code ([Vasiliev 2017](#)), which solves the time-dependent, isotropic Fokker-Planck equation for the energy-space distribution function  $f(\epsilon, t)$ . This equation can be written in flux-conserving form as

$$\frac{\partial f(\epsilon, t)}{\partial t} = - \frac{\partial}{\partial \epsilon} \left[ \underbrace{D_{\epsilon\epsilon} \frac{\partial f(\epsilon, t)}{\partial \epsilon} + D_{\epsilon} f(\epsilon, t)}_{F(\epsilon)} \right] - \frac{f(\epsilon, t)}{t_{\text{LC}}(\epsilon, t)} + S(\epsilon, t), \quad (2)$$

where  $\epsilon$  is the binding energy,  $D_{\epsilon}$  and  $D_{\epsilon\epsilon}$  are the first and second order energy diffusion coefficients,  $F(\epsilon)$  is the mass flux, and the last two terms account for the draining of stars into the loss cone of the SMBH (see eq. 13 in [Vasiliev 2017](#)), and injection of stars due to star formation. The diffusion coefficients can be expressed as integrals over the distribution function, which for a single species mass  $m$  are given by

$$D_{\epsilon\epsilon} = 16\pi^2 G^2 m \ln \Lambda \left[ h(\epsilon) \int_0^{\epsilon} f(\epsilon') d\epsilon' + \int_{\epsilon}^{\epsilon_{\text{max}}} f(\epsilon') h(\epsilon') d\epsilon' \right] \quad (3)$$

$$D_{\epsilon} = -16\pi^2 G^2 m \ln \Lambda \int_{\epsilon}^{\epsilon_{\text{max}}} f(\epsilon') g(\epsilon') d\epsilon', \quad (4)$$

where  $h(\epsilon)$  is the phase volume and  $g(\epsilon) = dh(\epsilon)/d\epsilon$  is the density of states (see e.g. [Merritt 2013](#)). For a Keplerian potential,  $h \propto \epsilon^{-3/2}$  and  $g \propto \epsilon^{-5/2}$ .

The one-dimensional Fokker-Planck approach is computationally efficient and reproduces the results from two-dimensional Fokker-Planck ([Cohn 1985](#); [Merritt 2015](#)) as well as Monte-Carlo and N-body calculations ([Vasiliev 2017](#)) reasonably well. A key assumption of this equation is spherical symmetry, which is in tension with the physical motivation for our source term  $S(\epsilon, t)$ : disk-mode star formation. However, it is reasonable to assume that compact remnants forming in a flattened, disk-like configuration will isotropize their orbital planes on timescales much shorter than a Hubble time. The most rapid isotropization process is probably vector resonant relaxation, which operates on timescales  $\sim 10^7$  yr at the radii of interest ([Kocsis & Tremaine 2011](#)). On longer timescales,  $\sim$  Gyr, two-body relaxation will isotropize orbital planes of disk stars. Furthermore, it is not at all clear if disk-mode star formation occurs in a preferred plane; if not, then the injected remnants from many different episodes of *in situ* star formation would naturally form with a quasi-isotropic angular distribution even absent relaxational processes. In principle, resonant relaxation ([Rauch & Tremaine 1996](#); [Hopman & Alexander 2006a](#)) may flatten the stellar density profile by causing stars to diffuse more rapidly into the loss cone. In practice, however, this effect only becomes important on small radial scales  $\lesssim 0.01 - 0.1$  pc ([Bar-Or & Alexander 2016](#)), interior to where most tidal captures occur.

Finally, strong gravitational scatterings by BHs can lead to significant evaporation of low mass stars and remnants from the cusp. This effect is not included in our models, but a post-hoc calculation shows it can make changes in the stellar density profile at levels  $\lesssim 40\%$  (see § 2.6).

### 2.3 Evolution with Compact Remnants Only

Compact objects which are injected near the present disk of massive stars at  $\sim 0.3$  pc will diffuse outwards via two-body scattering. To study this process, we solve eq. (2) with a constant source function of injected BHs,  $\dot{N}_{\text{bh}} = 2 \times 10^{-5} \text{ yr}^{-1}$ , corresponding to our “Fiducial $\times 10$ ” model. To whet our intuition in a controlled setting, we initially neglect contributions to the gravitational potential or diffusion coefficients from the background of NSs and stars.

Figure 1 (top panel) shows the resulting BH number density profile  $n(r)$  after 10 Gyr of evolution, over which a quasi-steady state is achieved on small radial scales. For comparison, a dashed line shows how little the solution changes if one neglects the gravitational potential of the stellar mass BHs and the loss cone sink (the final term in eq. 2). The steady-state BH profile is well described by a broken power law, with  $n \propto r^{-7/4}$  at small radii  $r \ll r_i$  and  $n \propto r^{-5/2}$  at  $r \gg r_i$ . As we now describe, these power-law slopes and the normalization of the BH profile can be understood through basic analytic arguments.

Compact objects injected at  $r_i$  diffuse outwards on the two-body relaxation timescale, which for a single mass population  $m_c$  is approximately given by<sup>6</sup>,

$$t_{\text{rx}} \approx \frac{0.34}{\log \Lambda} \frac{\sigma^3(r)}{G^2 n(r) m_c^2}, \quad (5)$$

where  $\sigma(r)$  is the one dimensional velocity dispersion,  $n(r)$  is the number density profile, and  $\log \Lambda \approx 15$  is the Coulomb logarithm.

In steady state, the formation rate of compact objects per unit volume equals the rate of outwards diffusion, i.e.

$$\frac{\dot{N}}{r_i^3} \sim \frac{n_i}{t_{\text{rx}}(r_i)}. \quad (6)$$

This implies a steady-state density at the injection radius of

$$n(r_i) \propto r_i^{-9/4} \dot{N}^{1/2} M^{3/4} m_c^{-1}, \quad (7)$$

where in taking  $\sigma \propto (GM/r)^{1/2}$  we have assumed that the SMBH of mass  $M$  dominates the gravitational potential. Normalizing equation (7) using results from our numerical solutions, we find

$$n_i = 1.6 \times 10^4 \left( \frac{r_i}{0.3 \text{ pc}} \right)^{-9/4} \left( \frac{\dot{N}}{2 \times 10^{-5} \text{ yr}^{-1}} \right)^{1/2} \left( \frac{M}{4 \times 10^6 M_\odot} \right)^{3/4} \left( \frac{m_c}{10 M_\odot} \right)^{-1} \text{ pc}^{-3}, \quad (8)$$

What sets the power-law slopes of the BH density profile?

<sup>6</sup> For a Keplerian potential, the pre-factor of eq. (5) varies from 0.2–0.4, depending on the density profile power-law slope  $\gamma$  = 0.5–3, where  $n \propto r^{-\gamma}$ .

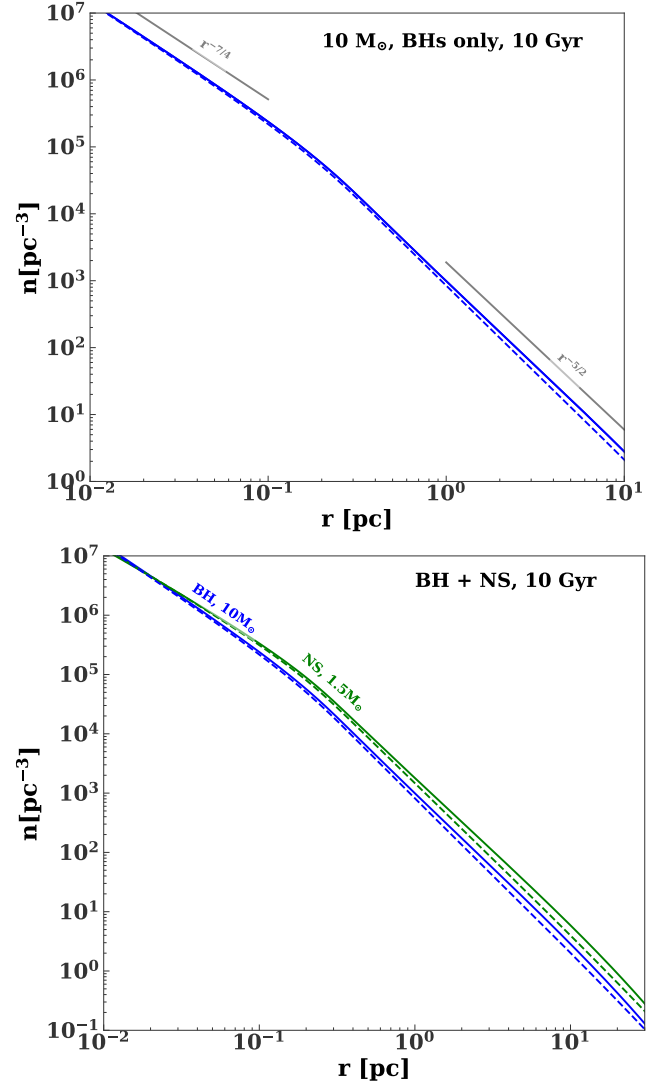


**Figure 1.** *Top panel:* Number density of BHs in the GC as a function of radius  $r$  after 10 Gyr of evolution, in the case of continuous BH injection (*solid line*). BHs are injected at a constant rate  $\dot{N}_{\text{bh}} = 2 \times 10^{-5} \text{ yr}^{-1}$  at  $r_{\text{in}} \approx 0.3$  pc. *Bottom panel:* Density profiles of NSs and BHs after 10 Gyr of evolution for injection rates at  $r_{\text{in}}$  corresponding to our Fiducial model ( $\dot{N}_{\text{ns}} = 4 \times 10^{-5}$ ,  $\dot{N}_{\text{bh}} = 2 \times 10^{-5} \text{ yr}^{-1}$ ). Dashed lines show how the results change if the gravitational potential of the compact objects, and the sink term due to SMBH loss cone, are neglected.

For a distribution function  $f \propto \epsilon^p$  which extends to a maximum energy  $\epsilon_{\text{max}}$ , the flux of mass through energy space (see eq. 2) is

$$F(\epsilon) \propto \epsilon^{2p-3/2} \left[ a_o(p) + a_1(p) \left( \frac{\epsilon_{\text{max}}}{\epsilon} \right)^{p-3/2} + a_2(p) \left( \frac{\epsilon_{\text{max}}}{\epsilon} \right)^{p-1/2} \right] \\ a_o(p) = \frac{3(4p-1)}{(1+p)(2p-1)(2p-3)}, \quad (9)$$

where  $a_1$ ,  $a_2$ , and  $a_3$  are dimensionless functions of  $p$ .

In steady state, the flux through energy space is constant. For  $p < 1/2$ , one finds  $F \approx a_o(p) \epsilon^{2p-3/2}$  in the limit that  $\epsilon_{\text{max}} \rightarrow \infty$  and thus  $F$  will be zero for  $p = 1/4$ ; this is the classical “Bahcall-Wolf” (BW) solution (Bahcall & Wolf

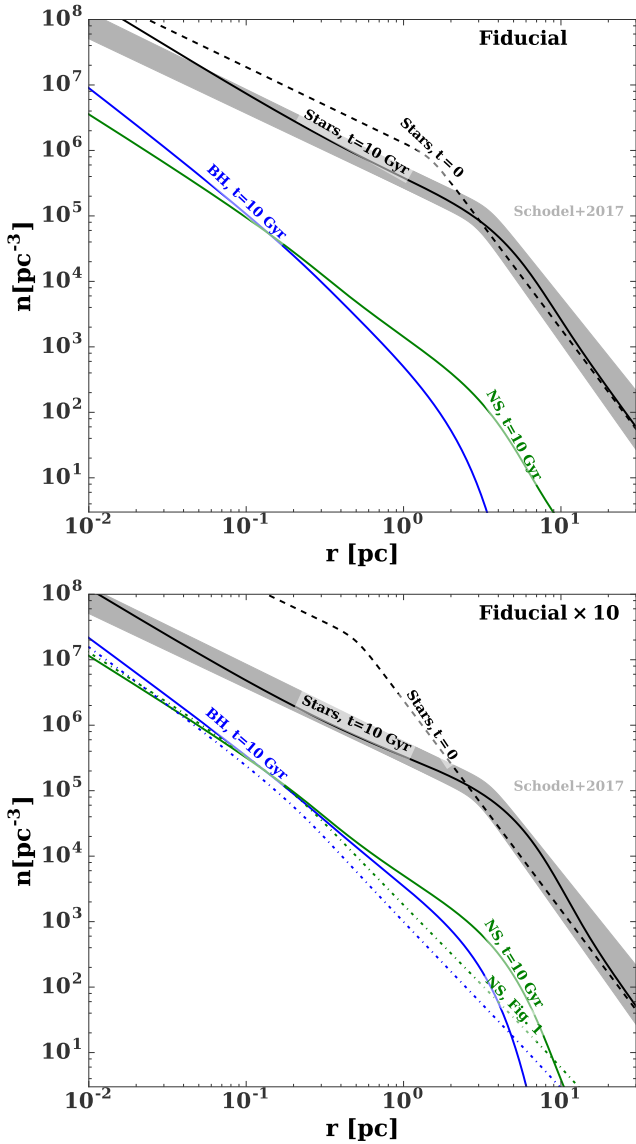


**Figure 2.** *Top panel:* Density profiles of stars and compact remnants at  $t = 10$  Gyr (solid lines), in the case that compact remnants are continually injected near  $\sim 0.3$  pc at the rates corresponding to the Fiducial model. The initial profile of stars is shown as a dashed black line, while the present-day distribution of low mass stars from Schödel et al. (2018) is shown as the shaded region (including uncertainties). *Bottom panel:* Density profiles of stars and compact objects in our Fiducial $\times 10$  model. For comparison, dash-dotted blue and green lines show, respectively the profiles of BHs and NSs, neglecting the pre-existing background of low mass stars/NSs (Fig. 1).

1976). If  $p > 1/2$ , then the  $a_2$  term in equation (9) dominates over the first two terms. The  $p = 1$  profile corresponds to the steady-state solution for a constant, non-zero (outwards) flux. In this case  $\epsilon_{\max}$  must have a finite value, as otherwise the flux would diverge; in our case, this maximum energy corresponds to the location of the source function of injected BHs at  $r_{\text{in}}$ . These two steady state solutions (zero

flux at small radii and constant outward flux<sup>7</sup> at large radii) correspond to density profiles  $n \propto r^{-7/4}$  and  $\propto r^{-5/2}$ , respectively.

The enclosed mass  $\propto nr^3 \propto r^{1/2}$  is dominated by the largest radius out to which the BHs have had time to diffuse over the system age  $t$ . The half-mass radius  $r_{1/2}$ , interior to which the above steady-state profile is established, can be estimated by equating  $t = t_{\text{rx}}$ ; using equation (5), this gives

$$r_{1/2} \approx 3.3 \text{ pc} \left( \frac{t}{3 \text{ Gyr}} \right)^2 \left( \frac{r_i}{0.3 \text{ pc}} \right)^{-1/2} \left( \frac{\dot{N}}{2 \times 10^{-5} \text{ yr}^{-1}} \right) \left( \frac{M}{4 \times 10^6 M_{\odot}} \right)^{-3/2} \left( \frac{m_c}{10 M_{\odot}} \right)^2. \quad (10)$$

BHs injected in the GC therefore have sufficient time to establish a steady-state profile within the central parsec by the present age ( $t = 10$  Gyr).

The bottom panel of Fig. 1 shows the present-day density profiles for a calculation otherwise identical to the BH-only case, but including the evolution of *both* the BHs and NSs, assuming each are injected at  $r_i$  at rates of  $\dot{N}_{\text{bh}} = 2 \times 10^{-5} \text{ yr}^{-1}$  and  $\dot{N}_{\text{ns}} = 4 \times 10^{-5} \text{ yr}^{-1}$ , respectively (the old population of stars and their associated NSs are still neglected). The addition of NSs has little effect on the BH profile compared to the BH-only case. Outside of the injection radius, the slope of the NS density profile is similar to the BH one, but with a greater overall normalization reflecting the relatively higher NS injection rate. At radii  $\lesssim r_i$ , the BH density profile approaches the BW shape  $n \propto r^{-7/4}$  (as in the BH-only case), while the NSs achieve a shallower profile  $\propto r^{-3/2}$ . A shallower profile for the lighter species is expected for a two-component model in which the heavy species dominates the diffusion coefficients (Bahcall & Wolf 1977; Alexander & Hopman 2009).

The analytic arguments presented above are readily extended to the multi-species case. In particular, the BH density at  $r_i$  can again be estimated by replacing the single remnant mass  $m_c$  in eq. (7) with a weighted generalization

$$\tilde{m} = \left( \frac{\dot{N}_{\text{bh}} m_{\text{bh}}^2 + \dot{N}_{\text{ns}} m_{\text{ms}}^2}{\dot{N}_{\text{bh}} + \dot{N}_{\text{ns}}} \right)^{1/2}. \quad (11)$$

## 2.4 Effects of stellar background and potential

We now explore the effects of also including the old population of low mass stars and NSs on the NSC evolution, the final step in constructing our NSC models. Fig. 2 shows the profile of stars, NSs, and BHs at  $t = 10$  Gyr in our Fiducial (top panel) and Fiducial $\times 10$  (bottom panel) models. BHs and NSs dominate the mass density inside of 0.03 (0.4) pc in the Fiducial (Fiducial $\times 10$ ) model.

The cusp of compact remnants causes the star cluster to expand radially over time, motivating our choice of a more

<sup>7</sup> This solution is related to the  $n \propto r^{-9/4}$  solution identified by Peebles (1972). Our profile is slightly steeper due to energy transfer from small to large scales by stars on eccentric orbits. However, Fragione & Sari (2017) have argued that this small minority of stars cannot effectively conduct energy to the bulk of the stellar population and would evolve in a decoupled way, in which case the slightly shallower Peebles' solution would be more accurate.

compact initial stellar profile (black dashed line) than the currently-observed one (shaded gray region; Schödel et al. 2018). By contrast, the compact objects become slightly more centrally concentrated than in the previous models where the stars were neglected (Fig. 1). There are two reasons for this: (i) stars tend to scatter the higher mass compact objects to larger binding energies (ii) the gravitational potential of the stars suppresses outward diffusions of compact objects.

## 2.5 Non-fiducial NSC Models

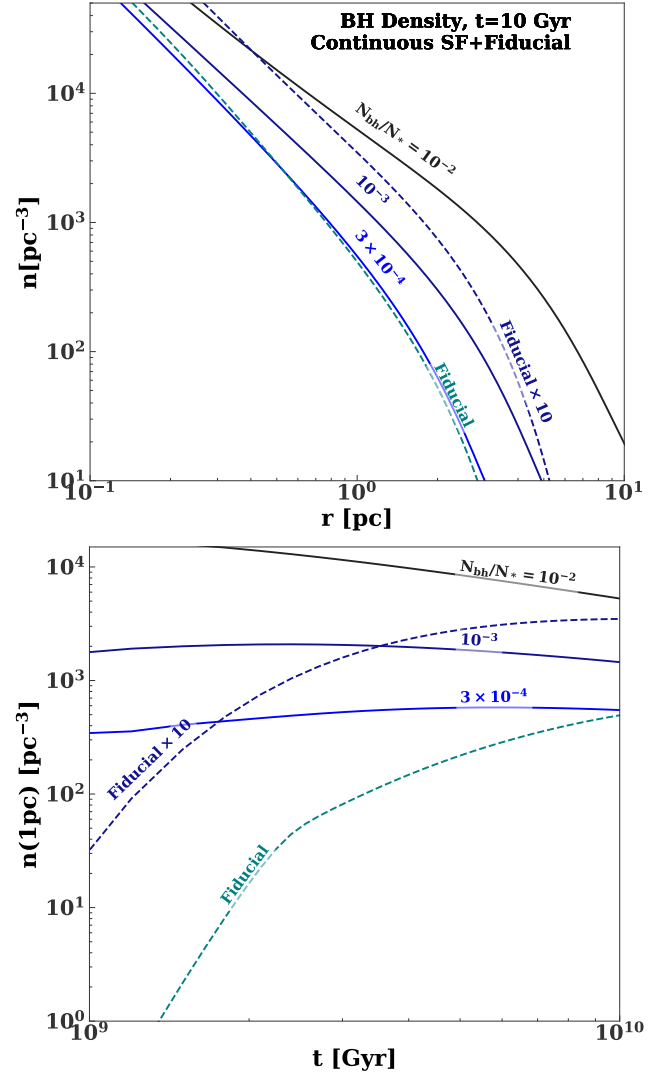
This section explores hypothetical (“non-fiducial”) scenarios for creating the GC’s NSC, in which all of the stars and compact objects instead form as a single population with a common density profile and standard IMF. These models are unrealistic for our own GC because they neglect the preferential injection of compact objects on small scales. They nevertheless represent useful limiting cases and allow us to compare our results to those of past work (e.g. Morris 1993; Miralda-Escudé & Gould 2000; Freitag et al. 2006). They are also useful for exploring the sensitivity of our results to the star formation history, and for generalizing them to other galactic nuclei with other histories (Leigh et al. 2016). These non-fiducial scenarios are summarized in Table 2.

Fig. 3 shows the BH profile at  $t = 10$  Gyr which results if both stars and compact remnants are formed impulsively at  $t = 0$  (initial scale radius of  $r_o = 1$  pc) and assuming no subsequent star formation. We show results for a range of models which assume different ratios for the number of stars to compact objects,  $N_{bh}/N_*$ . For a Kroupa IMF in which BHs originate from stars of mass  $\gtrsim 25M_\odot$ , we expect  $N_{bh}/N_* \sim 10^{-3}$ , which (coincidentally) coincides with the number of BHs injected by the present day in our Fiducial $\times 10$  model. However, because the BHs in this case are injected directly at small radii, their density at radii  $\lesssim 1$  pc in our Fiducial $\times 10$  models exceeds the primordial model with  $N_{bh}/N_* = 10^{-3}$  by a factor of a few.

Fig. 4 shows the BH density profile under the assumption that they form continuously at a constant rate over the age of the NSC, with a spatial profile identical to the present-day stellar population. The BH density at small radii  $\lesssim 1$  pc evolves significantly over time, taking several Gyr to reach a quasi-steady state.

Our previous scenarios assumed the central SMBH possesses a fixed mass,  $4 \times 10^6 M_\odot$ . However, if the NSC is built up by continuous star formation, then the SMBH may grow in concert with the cluster through gaseous accretion or star capture. Fig. 5 shows the density profiles of stars and compact objects at  $t = 10$  Gyr if the SMBH mass is artificially fixed at all times to be 7% of the mass of the NSC. This speeds up the evolution because the velocity dispersion, and hence the cluster relaxation timescale (eq. 5) is smaller at early times. Nevertheless, the final distribution of BHs is similar to the previous cases (cf. Fig. 4).

Overall, we find that the final distribution of remnants after  $\sim 10$  Gyr is mostly sensitive to the overall rate of production of BHs versus stars, and is rather insensitive to the details of the star formation history, or its precise radial distribution within the NSC.



**Figure 3.** *Top panel:* Density profile of BHs at 10 Gyr for different star formation histories (Table 2). Solid lines show non-fiducial models in which the BHs form impulsively at  $t = 0$  with the same profile as the stars (eq. 1), with colors labeling the ratio of BHs to stars. For comparison, dashed lines show our Fiducial and Fiducial $\times 10$  models, in which the BHs are instead injected continuously at small radii (see Fig. 2 and surrounding discussion). *Bottom panel:* Time evolution of the BH density at  $r = 1$  pc for each of the formation histories shown in the top panel.

## 2.6 Effects of strong scattering

So far we have neglected BHs ejecting stars via strong scatterings in our models. In this section we quantify this effect, which under some circumstances can be important for bulk cluster evolution (Lin & Tremaine 1980). The volumetric ejection rate at radius  $r$  is

$$\dot{n}_{ej}(r) = n_{bh}(r)n_*(r)\langle\Sigma(v_\infty)v_\infty\rangle \quad (12)$$

where  $n_{bh}(r)$  is the number density of BHs,  $n_*(r)$  is the stellar density,  $v_\infty$  is relative velocity at infinity,  $\Sigma(v_\infty)$  is the cross-section for ejection, and the angle brackets denote an average over the relative velocity distribution. This expression may be rewritten as

**Table 2.** Summary of models for assembling the populations of stars and compact remnants in the GC. The top two rows summarize our “fiducial” models, in which low mass stars and NSs are initialized at  $t = 0$  following a radial profile given by eq. (1) with the scale radius  $r_0$  and NS-to-star number ratio  $N_{\text{ns}}/N_{\star}$ . BHs and NSs are also continuously injected inside of  $\sim 0.3$  pc, near the outer edge of the observed young stellar disks, with rates  $\dot{N}_{\text{bh}}$  and  $\dot{N}_{\text{ns}}$ , respectively. The bottom three rows summarize other, non-fiducial scenarios, in which all compact remnants and stars form with the same radial distribution, either impulsively in the distant past or continuously. The masses of the stars, NSs, and BHs, are taken to be  $0.3M_{\odot}$ ,  $1.5M_{\odot}$ , and  $10M_{\odot}$ , respectively.

Scenario	$r_o$ [pc]	$N_{\star}(t=0)$	$\dot{N}_{\star}$ [yr $^{-1}$ ]	$N_{\text{bh}}/N_{\star}(t=0)$	$N_{\text{ns}}/N_{\star}(t=0)$	$\dot{N}_{\text{bh}}$ [yr $^{-1}$ ]	$\dot{N}_{\text{ns}}/\dot{N}_{\text{bh}}$	$M_{\bullet}$	Fig.
Fiducial	1.5	$1.9 \times 10^8$	–	–	$10^{-3}$	$2 \times 10^{-6}$	2	$4 \times 10^6 M_{\odot}$	2
Fiducial $\times 10$	0.5	$1.9 \times 10^8$	–	–	$10^{-3}$	$2 \times 10^{-5}$	2	$4 \times 10^6 M_{\odot}$	2
Impulsive	1	$1.9 \times 10^8$	–	$3 \times 10^{-4}, 10^{-3}, 10^{-2}$	$4N_{\text{bh}}/N_{\star}$	–	–	$4 \times 10^6 M_{\odot}$	3
Continuous SF Existing SMBH	3	–	$1.9 \times 10^{-2}$	$3 \times 10^{-4}, 10^{-3}, 10^{-2}$	$4N_{\text{bh}}/N_{\star}$	–	–	$4 \times 10^6 M_{\odot}$	4
Continuous SF Growing SMBH	3	–	$1.9 \times 10^{-2}$	$3 \times 10^{-4}, 10^{-3}, 10^{-2}$	$4N_{\text{bh}}/N_{\star}$	–	–	7% $M_{\text{tot}}$	5

$$\dot{n}_{\text{ej}} = I(m_c/m_{\star})n_{\text{bh}}(r)n_{\star}(r)\sigma(r)\pi b_o^2$$

$$b_o = \frac{G(m_c + m_{\star})}{\sigma(r)^2} \quad (13)$$

where  $m_c$  and  $m_{\star}$  are the masses of the compact object and star respectively,  $\sigma(r)$  is the (1D) velocity dispersion of the compact objects. The likelihood of ejection increases with the mass of the compact object, as quantified by the dimensionless number  $I$ . In an encounter, the change in the star’s velocity is given by

$$\Delta v_{\parallel} = \frac{-2v_{\infty}}{1+x^2} \frac{m_c}{m_c + m_{\star}} \quad (14)$$

$$\Delta v_{\perp} = \frac{2v_{\infty}x}{1+x^2} \frac{m_c}{m_c + m_{\star}} \quad (15)$$

$$x = \frac{bv_{\infty}^2}{G(m_c + m_{\star})} \quad (16)$$

where the first and second lines are the components parallel and perpendicular to the initial relative velocity. The change in the star’s specific energy is

$$\Delta E = \frac{1}{2}\Delta v^2 + \Delta \mathbf{v} \cdot \mathbf{v}_{\star} \quad (17)$$

where  $\mathbf{v}_{\star}$  is the star’s initial velocity. For a star to be ejected  $\Delta E$  should at least exceed the specific binding energy of the central SMBH, viz.

$$\Delta E \geq \frac{GM}{2r} = \frac{(1+\delta)}{2}\sigma(r)^2, \quad (18)$$

where  $\delta$  is the logarithmic BH density slope. To determine the normalization of the ejection rate, we compute a Monte Carlo ensemble of encounters with different relative velocities, approach angles, and impact parameters. Assuming a Maxwellian velocity distribution for the stars and black holes, a uniform distribution of the cosine of the approach angle, and  $\delta = 1.75$ , the numerical pre-factor ( $I$ ) in equation (13) is 0.1, 1, and 1.3 for  $m_c/m_{\star} = 1, 10$ , and 50 respectively (see also [Henon 1969](#)).

The total ejection rate may be dominated by stars on eccentric orbits. Considering a thermal eccentricity distribution increases the ejection rate by a factor  $\sim 3.7$  (relative to purely circular orbits, and assuming that the BH perturbers have an  $r^{-1.75}$  profile). Then, the ejection rate from strong

scatterings is

$$\dot{n}_{\text{ej}} \approx 3.7\pi I(m_c/m_{\star})n_{\star}(r)n_{\text{bh}}(r)\sigma(r)^{-3}G^2m_c^2$$

$$\approx 4n_{\star}(r)\ln\Lambda^{-1}t_{\text{rx,bh}}(r)^{-1}, \quad (19)$$

where  $\ln\Lambda \approx 15$  is the Coulomb logarithm and we take  $m_c/m_{\star} = 10$ . At any radius the time-scale for a star to be unbound from the central SMBH is approximately four times the local relaxation time of the BHs. To test how this effect would modify the stellar density, we add an additional sink term into PHASEFLOW. We find that the stellar density is modified by  $\lesssim 25\%$  ( $40\%$ ) outside of 0.01 pc in our Fiducial (Fiducial $\times 10$ ) models. The total number of stars ejected from the cusp is  $\sim 2.7 \times 10^6$  in the Fiducial model and  $7 \times 10^6$  in the Fiducial $\times 10$  model. These likely represent upper limits on the uncertainty caused by our neglect of strong scatterings, as Eq. 18 represents a generous ejection criterion.

### 3 TIDAL CAPTURE BINARY FORMATION

A close encounter between a star of mass  $m_{\star}$  and a compact object of mass  $m_c$  can lead to the formation of an XRB through tidal capture. During pericenter passage, tidal forces transfer orbital energy into stellar oscillations, capturing the star into an elliptical orbit.

The maximum initial pericenter distance which results in tidal capture,  $r_{\text{capt}}$ , can be estimated by equating the hyperbolic orbital energy with the energy deposited in tides (see Appendix D of [Stone et al. 2017b](#), and Appendix A in this paper). This condition can be expressed as

$$\mu \frac{v_{\infty}^2}{2} = \frac{Gm_{\star}^2}{r_{\star}} \left(\frac{m_c}{m_{\star}}\right)^2 \left(\frac{r_{\star}}{r_{\text{capt}}}\right)^6 T_2(r_{\text{capt}}, m_{\star}/m_c), \quad (20)$$

where  $r_{\star}$  is the stellar radius,  $\mu$  is the reduced mass, and  $T_2$  is the tidal coupling constant (we only include the dominant  $l = 2$  modes). For distant pericenters this may be estimated using the linear theory (see Appendix A and [Lee & Ostriker 1986](#)). However, for the closest pericenters relevant for capture, linear theory underestimates the tidal coupling constant by a factor of a few. The magnitude of non-linear effects has been estimated for polytropic models by [Ivanov & Novikov \(2001\)](#), and we adopt their prescriptions for close pericenters, as discussed in Appendix B.



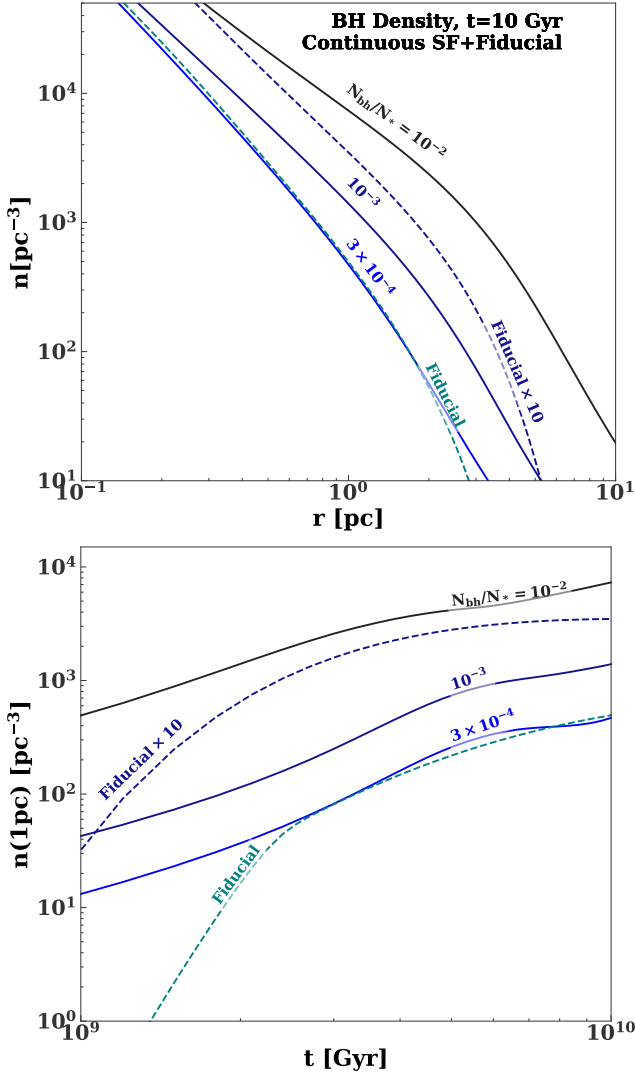


**Figure 4.** *Top panel:* Density profile of BHs at 10 Gyr under the assumption that the NSC is built up by continuous star formation at a constant rate with a spatial profile identical to the present-day stellar population; colors denote different ratios of BHs to stars,  $N_{\text{bh}}/N_{\star}$ . For comparison, dashed lines show the BH profile in our Fiducial and Fiducial $\times 10$  scenarios (Fig. 2). *Bottom panel:* Time evolution of the BH density at 1 pc, for each of the formation histories in the top panel.

Fig. 6 shows the maximum pericenter distance for tidal capture as a function of the relative velocity at infinity,  $v_{\infty}$ , normalized to the stellar escape speed,  $v_{\text{esc}} = \sqrt{2Gm_{\star}/r_{\star}}$ . The capture radius  $r_{\text{capt}}$  is typically  $\lesssim 2$  times greater than the characteristic tidal radius  $r_t \equiv r_{\star}(m_c/m_{\star})^{1/3}$ . Note that tidal capture cannot occur if  $v_{\infty} \gtrsim v_{\text{esc}}$  and thus is suppressed at small radii  $r \lesssim 0.1 - 1$  pc where the velocity dispersion is large; the same considerations virtually prohibit the tidal capture of giant stars in the GC. For even closer pericenter passages, inside of the so-called *disruption radius*  $r_{\text{dis}} \approx 0.5 - 1.1r_t$  (depending on stellar structure; Guillochon & Ramirez-Ruiz 2013), stars are tidally disrupted rather than captured.

The combined volumetric rate of tidal captures ( $r_{\text{dis}} \leq$

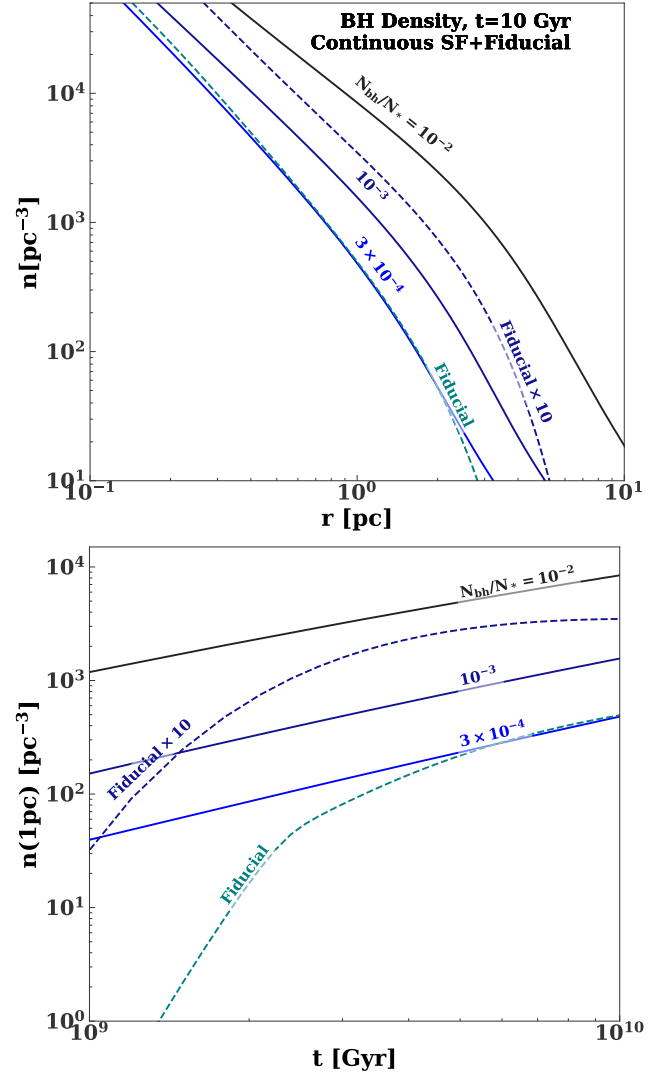


**Figure 5.** Same as Fig. 4, except the central SMBH is fixed to be 7% of the total cluster mass at all times, so that it grows with the cluster.

$r_{\text{p}} \leq r_{\text{capt}}$ ) and disruptions ( $r_{\text{p}} \leq r_{\text{dis}}$ ) at Galactocentric radius  $r$  is given by

$$\Gamma(r, t) = \int_0^{v_{\text{max}}(m_{\star})} n_c(r, t) n_{\star}(r, t) v_{\infty} \pi r_o^2 \times \left[ 1 + \frac{2G(m_c + m_{\star})}{r_o v_{\infty}^2} \right] f(v_{\infty}, r, t) dv_{\infty},$$

$$r_o = \max[r_{\text{capt}}(v_{\infty}, m_c/m_{\star}), r_{\text{dis}}(m_{\star})] \quad (21)$$

where  $n_c(r, t)$  is the number density of compact objects,  $n_{\star}(r, t)$  is the number density of stars, and  $f(v_{\infty})$  is the distribution of relative velocities. A hard upper limit to the value of  $v_{\text{max}}(m_{\star})$  is the stellar escape velocity (for faster relative velocities most of star would remain unbound from the compact object in any tidal interaction), but in practice  $v_{\text{max}}(m_{\star})$  is the relative velocity such that  $r_{\text{capt}} = r_{\text{dis}}$  in eq. (20). This may be smaller than stellar escape speed by a factor of  $\sim 2$ . We approximate the velocity distribution as a Maxwellian, with a scale parameter equal to the local ve-

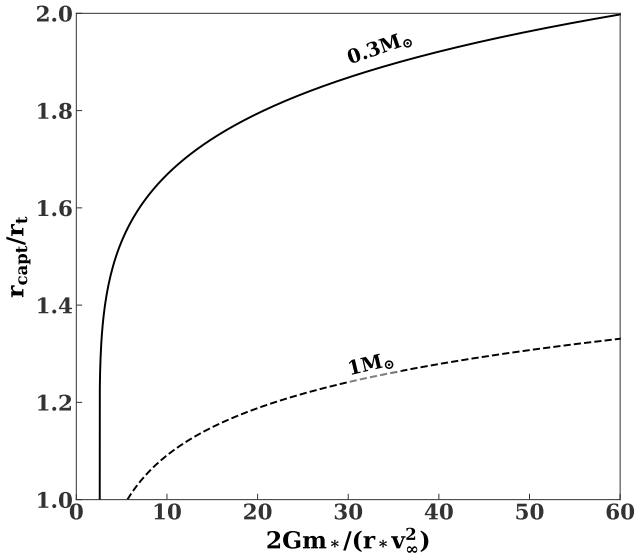


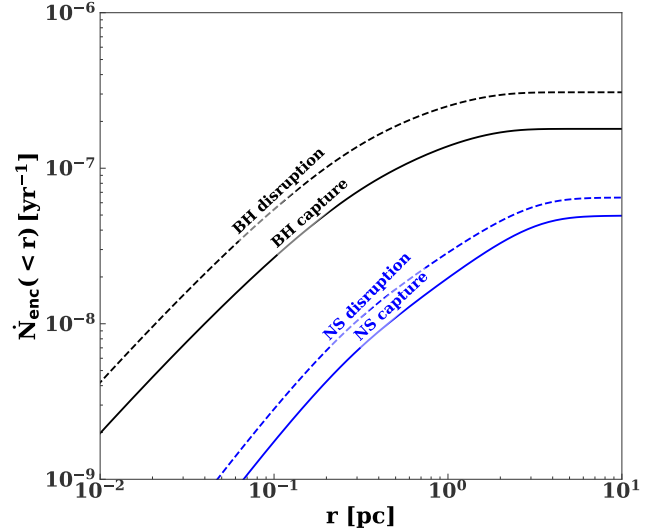
**Figure 6.** Maximum pericenter distance  $r_{\text{capt}}$  (normalized to the BH tidal radius  $r_t$ ) at which a main sequence star can be tidally captured by a BH of mass  $10M_{\odot}$ , as a function of the stellar escape speed (normalized to the relative velocity at infinity,  $v_{\infty}$ ). Results are shown for two stellar masses,  $0.3 M_{\odot}$  (solid line) and  $1 M_{\odot}$  (dashed line). The former is modeled as an  $n = 3/2$  polytrope and the latter is modeled as an  $n = 3$  polytrope.

locity dispersions of the two species added in quadrature.<sup>8</sup> The term in brackets allows for gravitational focusing, which exceeds the geometric cross section for  $r \gtrsim 0.01$  pc.

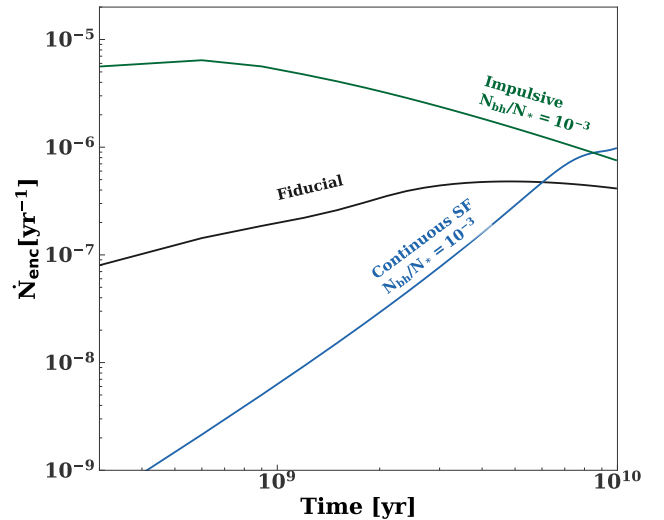
Fig. 7 shows our calculation of the present-day rate of total stellar tidal disruptions (dashed lines) and tidal captures (solid lines) by BHs and NSs, as calculated using the predictions of our Fiducial model for  $n_*$  and  $n_c$ . The capture/disruption rate by BHs exceeds that of NSs by a factor of  $\gtrsim 3 - 10$  across most radii of interest; this is partially because in the limit of gravitationally-focused collisions, the rate of captures/disruptions obeys  $\Gamma \propto m_c^{4/3}$ . The rate of tidal captures is somewhat smaller than the rate of disruptions, since for typical relative velocities capture occurs over a narrower range of pericenter distance than does disruption. Some tidal captures may lead to a series of partial disruptions instead of the formation of a stable binary, even if the initial pericenter is outside of the disruption radius (see the discussion in § 3.2).

Fig. 8 shows the tidal capture and disruption rate of stars by BHs as a function of time for different star formation histories corresponding to our Fiducial (§2.4) and non-fiducial scenarios (§2.5). In the Fiducial scenario, with compact remnant injection inside of  $\approx 0.3$  pc, the encounter rate increases for the first  $\sim 3$  Gyr, as the number of compact objects increases. The rate then declines slightly as the compact objects reach a steady state on small scales, while the population of pre-existing low mass stars are pushed out-

<sup>8</sup> In detail the velocity distribution in the Keplerian potential of the SMBH is not Maxwellian, but this is a good approximation for our model stellar density profiles (see e.g. Alexander & Kumar 2001).



**Figure 7.** Present-day cumulative rate of tidal disruptions (dashed lines) and tidal captures (solid lines) inside of radius  $r$  for our Fiducial scenario. A total of  $\approx 6 \times 10^{-7}$  strong tidal encounters occur per year.



**Figure 8.** Rate of strong tidal encounters (disruptions plus captures) as a function of time in our Fiducial model (§ 2.4) as well as two of the non-fiducial scenarios (§ 2.5).

wards to larger radii. The non-fiducial scenario with impulsive injection of compact remnants and stars shows qualitatively similar behavior, but with the encounter rate peaking much earlier in time. Finally, in the non-fiducial scenario of continuous star formation, the encounter rate monotonically increases.

### 3.1 Tidal Capture and Circularization

As described by Stone et al. (2017b), there are three possible outcomes of a tidal capture: (1) the star continues to lose energy at each pericenter passage, until its orbit is circular;

(2) the binary is perturbed by another star or compact object before circularization is complete; (3) the star inflates due to tidal heating, and is destroyed in a series of partial tidal disruptions.

Circularization of the binary can be interrupted (option 2) if the initial pericenter of the encounter is sufficiently large, in which case the tidal energy transfer is weak and the star barely captures into a highly elliptical orbit. In the limit of very large post-capture apocenter, an encounter with another star will perturb the orbital angular momentum faster than circularization can occur. Such encounters generally increase the angular momentum of the binary (since there is more phase volume at larger angular momenta), derailing the circularization process. However, comparing the time-scales for circularization and angular momentum diffusion (Stone et al. 2017b; their eqs. 21, 25), we find that circularization is slower than the outwards angular momentum diffusion time from stellar interactions for only a extremely narrow range of pericenters, within  $10^{-3}$  of the maximum value for capture. Only a tiny fraction of tidally captured binaries will be perturbed by a third star before they circularize.

Another hazard for a tidally captured star is a string of partial disruptions due to the energy deposited by tides and tidal stripping near pericenter. Complete destruction of the star is energetically allowed if the energy released during circularization  $E_{\text{circ}}$  exceeds the total (internal + gravitational binding) energy of the star  $E_*$ . As shown in Fig. 9, a star captured by a black hole necessarily has  $E_{\text{circ}} \gtrsim E_*$  (e.g. Kochanek 1992; Alexander & Morris 2003). The energy required for a star to circularize around a NS is smaller than the BH case, but still can be comparable to the energy of a low mass star.

However, even if  $E_{\text{circ}} \gtrsim E_*$ , this does not necessarily mean the star will be destroyed. If a significant fraction of the mode energy is deposited near the stellar surface, then it could be radiated away or carried outwards by a wind (Fuller & Lai 2011, 2012; Wu 2017). Whatever remains of the star following this process would then still circularize, albeit with a potentially lower mass and higher entropy than its original state prior to being captured.

The star will lose mass during the circularization process (either due to mode dissipation or direct dynamical stripping at pericenter). The time-scale for mass loss is shorter than the thermal time-scale of the star and its radius will grow adiabatically (Linial & Sari 2017). As the star grows tidal dissipation becomes stronger, potentially leading to run-away heating and disruption of the star (Kochanek 1992). However, if the mass loss occurs primarily from the side of star closer to the compact object, the pericenter can grow faster than the stellar radius averting the run-away.

Another important issue is the time-scale over which the mode energy deposited into the star is dissipated. Mardling (1995) has argued that a tidally captured star necessarily undergoes a random walk in eccentricity, since mode oscillations from consecutive pericenter passages would interfere with each other, leading to chaotic exchange of energy between the orbit and the star that would likely lead to the latter's disruption. However, this will not occur if the mode energy is dissipated over the course of a single orbit. This can plausibly occur via non-linear mode-mode couplings (Kumar & Goodman 1996), especially for the large amplitude modes

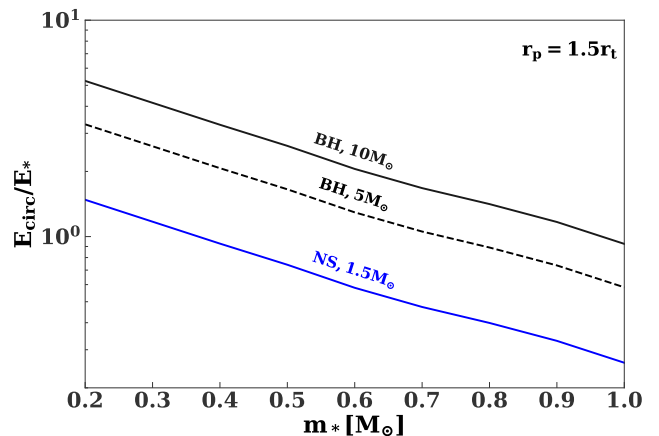


**Figure 9.** Ratio of the required to circularize the star into a binary with a NS or BH ( $E_{\text{circ}}$ ) to the total (internal + gravitational binding) energy of the star ( $E_*$ ) as a function of stellar mass. Although  $E_{\text{circ}} \gtrsim E_*$  across much of the parameter space, tidal capture is not necessarily fatal for the star because the circularization energy can be deposited by modes primarily in the outer layers of the star, where it is likely to drive non-destructive mass loss.

that will be excited by tidal capture in the GC, where the energy deposited into the star on the first pericenter passage is  $\gtrsim 10^{47}$  erg. For example, Kumar & Goodman (1996) show that the  $f$ -modes excited in low mass stars can dissipate energy on a time-scale of  $30 (E/10^{45} \text{ erg})$  days, where  $E$  is the energy deposited into the star. This would be shorter than the orbital period of a captured low mass star ( $\gtrsim 5$  days). Higher mass stars can dissipate energy even more efficiently by resonantly exciting  $g$ -modes, and nonlinear oscillations may dissipate their energy even faster by steepening into shocks.

The long-term evolution of a highly eccentric tidal capture binary remains an open question, and its solution is beyond the scope of this work. For the remainder of this paper, we assume that tidal capture binaries are in fact able to circularize without being destroyed, but this assumption must be examined in future modeling.

### 3.2 X-ray Binary Formation and Evolution

Once the star circularizes into an orbit around the compact object, the binary semi-major axis  $a$  will be roughly twice the pericenter radius of the captured star.<sup>9</sup> The orbit will then decay over long timescales due to gravitational wave

<sup>9</sup> The relation  $a = 2r_p$  will be exact if angular momentum and mass are conserved during circularization, except for a small correction for stellar spin (Lee & Ostriker 1986).

emission<sup>10</sup>, such that  $a$  decreases according to

$$\frac{\dot{a}}{a} = 2 \frac{\dot{J}_{\text{GW}}}{J} = -\frac{64}{5} \frac{G^3}{c^5} \frac{m_* m_c (m_* + m_c)}{a^4}. \quad (22)$$

Here  $J$  is the circular orbit angular momentum, and  $\dot{J}_{\text{GW}}$  is the quadrupole-order rate of angular momentum radiation (Peters 1964). Once the system enters Roche-lobe contact, the subsequent evolution of the semi-major axis and mass accretion rate onto the compact object obey (e.g. Frank et al. 2002)

$$\begin{aligned} \frac{\dot{m}_*}{m_*} &= \frac{\dot{J}_{\text{GW}}}{J} \left[ 1.2 - \frac{m_*}{m_c} \right]^{-1} \\ \frac{\dot{a}}{a} &= 2 \frac{\dot{J}_{\text{GW}}}{J} - 2 \frac{\dot{m}_*}{m_*} \left( 1 - \frac{m_*}{m_c} \right), \end{aligned} \quad (23)$$

where we have assumed the star maintains thermal equilibrium, i.e. that its radius follows the main-sequence,  $r_* \propto m_*^{0.8}$ .

Fig. 10 shows the binary lifetime after the star enters Roche-Lobe contact as a function of the masses of the star and compact remnant. The lifetime is defined as the interval over which (1) the star has not yet evolved off the main sequence and (2) the star’s mass still exceeds  $0.1M_\odot$ . The last condition is motivated by the fact that once  $m_* \lesssim 0.1M_\odot$  the star’s equation of state changes, resulting in a one to two order of magnitude reduction in the mass-transfer rate (and an undetectably dim X-ray source). Likewise, if the star evolves off the main sequence, the star and compact object may undergo a common envelope phase, with an outcome that is uncertain theoretically.

Fig. 10 shows that the binary lifetime decreases for larger compact object masses, due to more rapid evolution through gravitational wave emission. For low-mass stars ( $m_* \lesssim 1M_\odot$ ), the binary lifetime also increases with  $m_*$  because the tidal radius (and thus the initial separation) is larger for higher mass stars. For massive stars ( $m_* \gtrsim 1M_\odot$ ), the binary lifetime is instead limited by the main-sequence lifetime.

The present-day ( $t = t_h = 10$  Gyr) density of XRBs at radius  $r$  is approximately given by<sup>11</sup>

$$n_x(r) = \int_0^{t_h} \int_{r_{\text{min}}(t)}^{r_{\text{max}}(t)} d\Gamma(r_p, r, t) dr_p dt, \quad (24)$$

<sup>10</sup> In principle spin-down by magnetic braking also contributes to angular momentum losses from the star. However, there is considerable uncertainty in the spin-down rate for high rotation speeds in contact binaries. Empirically, magnetic braking is sub-dominant to gravitational wave emission in BH binaries, as otherwise one predicts a population of bright, persistent short period BH LMXBs that are not observed (see Yungelson et al. 2006; Ivanova & Kalogera 2006). By analogy with cataclysmic variables, magnetic braking is likely also sub-dominant in NS systems with periods  $\lesssim 3$  hours.

<sup>11</sup> Eq. (24) implicitly assumes that binaries are visible as XRB at the radii where they are formed. In reality, binaries radially diffuse over time after forming, an effect we quantify in Fig. 12.

where

$$\begin{aligned} d\Gamma(r_p, r, t) &= n_c(r, t) n_*(r, t) \sigma 2\pi r_p \times \\ &\left[ I_0(r_p, \sigma) + \frac{G(m_c + m_*)}{\sigma^2 r_p} I_1(r_p, \sigma) \right] \\ I_0(r_p, \sigma) &= \int_0^{v_\infty(r_p)} \frac{v_\infty}{\sigma} f(v_\infty) dv_\infty \\ I_1(r_p, \sigma) &= \int_0^{v_\infty(r_p)} \frac{\sigma}{v_\infty} f(v_\infty) dv_\infty, \end{aligned} \quad (25)$$

is the capture rate per unit pericenter,  $v_\infty(r_p)$  is the maximum relative velocity that would result in a capture (the second term in the brackets dominates). The limits of integration in eq. 24 are the minimum and maximum initial pericenters for which the binary would be active today.

For close pericenters, the star loses a significant fraction of its mass via direct tidal stripping, leading to the star’s destruction in a series of partial disruptions. Quantitatively, Ivanov & Novikov (2001) find that an  $n = 3/2$  (3) polytrope would lose 10% of its mass for a pericenter of  $1.5$  (1)  $r_t$ . Based on these results we also require

$$r_p > \begin{cases} 1.5r_t, & m_* \leq 0.7M_\odot \\ r_t, & m_* > 0.7M_\odot \end{cases}. \quad (26)$$

To accurately calculate the tidal capture rate at small Galactocentric radii (where the rate becomes zero for stellar velocities equal to the local velocity dispersion  $\sigma$ ), we must integrate over the velocity distribution. For a Maxwellian velocity distribution, the integrals over relative velocity in the rate can be evaluated analytically:

$$\begin{aligned} I_0(r_p, \sigma) &= \sqrt{\frac{2}{\pi}} \left[ e^{-\frac{v_\infty(r_p)^2}{2\sigma^2}} \left( -\frac{v_\infty(r_p)^2}{\sigma^2} - 2 \right) + 2 \right] \\ I_1(r_p, \sigma) &= \sqrt{\frac{2}{\pi}} \left( 1 - e^{-v_\infty(r_p)^2/2\sigma^2} \right). \end{aligned} \quad (27)$$

Fig. 11 shows our calculation of the cumulative tidal capture rate inside radius  $r$ , using our Fiducial model for the time-dependent density profiles of BHs, NSs, and stars (Fig. 2). We explore the dependence of the capture rate on stellar mass by fixing the number density of the stars, but varying their mass  $m_*$ . The *per star* capture rate is larger for higher mass stars due to their larger tidal radii; however, lower mass stars are more numerous for any realistic mass function and thus dominate the total number of formed binaries.

Fig. 12 shows our fiducial model predictions for the present-day total number of accreting BH and NS XRBs interior to a given radius. Dashed lines show the initial radial distribution of the binaries just after forming, while the solid lines show the distribution they would achieve if given sufficient time to relax in the cluster potential. To calculate the latter, we first find the previous time snapshot with a look-back time equal to the mean binary lifetime. Then, we insert a “tracer” population of binaries with the expected initial distribution, and evolve the system forward in time.

Table 3 summarizes the predictions of our fiducial models for the number of tidally-captured XRBs in the central parsec of our GC. The average accretion rate for BH (NS) binaries is  $10^{-10}$  ( $3 \times 10^{-11}$ )  $M_\odot \text{ yr}^{-1}$ , corresponding to  $5 \times 10^{-4}$  ( $10^{-3}$ ) of the Eddington rate  $\dot{M}_{\text{Edd}} = L_{\text{Edd}}/0.1c^2$ , where  $L_{\text{Edd}} = 1.3 \times 10^{38} (m_c/M_\odot) \text{ erg s}^{-1}$  is the Eddington

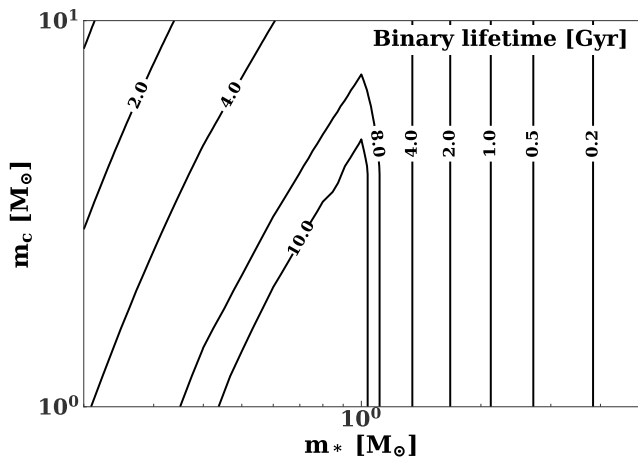


**Figure 10.** Binary lifetime after Roche-Lobe contact is reached as a function of the stellar mass ( $m_*$ ) and compact object mass ( $m_c$ ). The binary lifetime is defined as the interval over which the following criteria are met: (1) the companion mass still exceeds  $0.1 M_\odot$  and (2) the star has not evolved off the main sequence. We use equation 5 from Hurley et al. (2000) for the main sequence lifetime (and assume a solar metallicity star).

luminosity. These accretion rates are generally less than the theoretical critical threshold value below which the disk is thermally unstable,

$$\dot{M}_{\text{crit}} \approx 3.2 \times 10^{-11} M_\odot \text{ yr}^{-1} \left( \frac{m_c}{M_\odot} \right)^{0.5} \left( \frac{m_*}{M_\odot} \right)^{-0.2} \times \left( \frac{P}{1 \text{ hour}} \right)^{1.4}, \quad (28)$$

where  $m_c$ ,  $m_*$ , and  $P$  are the mass of the compact object, mass of the donor star, and period of the orbit, respectively (Dubus et al. 1999). Thus, we expect XRBs formed by tidal capture to be transient sources, with long quiescent periods interspersed with bright outbursts.

## 4 X-RAY OBSERVATIONS

Hailey et al. (2018) discovered twelve new non-thermal X-ray sources in the central parsec of our galaxy. Of these, six are solid BH-XRB candidates, while the identity of the remainder is less certain (they may be either additional XRBs or MSPs). In principle, many more sources may be present with luminosities below the *Chandra* detection threshold of  $L_x \approx 4 \times 10^{31} \text{ erg s}^{-1}$ . Indeed, field BH-XRBs are known with luminosities as low as  $L_x \approx 2 \times 10^{30} \text{ erg s}^{-1}$  (Armas Padilla et al. 2014). To estimate the total number of unobserved XRBs lurking in the central parsec, Hailey et al. (2018) first estimate what the flux of the minimum luminosity source from Armas Padilla et al. (2014) would be if it were in the GC (accounting for absorption and instrumental response). Then, extrapolating the observed luminosity function ( $N(> F) \propto F^{-\alpha}$ ,  $\alpha = 1.57 \pm 0.16$ ) to this flux, they conclude that the total number of XRBs could be as high as 400–1000.

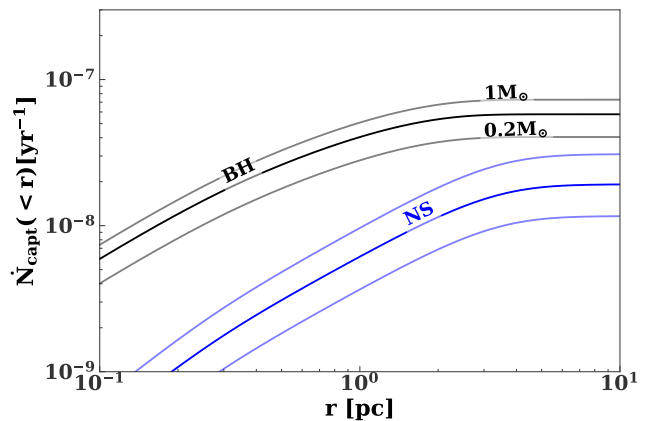


**Figure 11.** Present-day binary formation rate from tidal captures of low mass stars by BHs (black lines) and NSs (blue lines) interior to a given Galactocentric radius  $r$ , as calculated using our Fiducial model for the population of stars and compact remnants in the GC (Fig. 2). The thin lines show models in which we have fixed the stellar density but consider a single-mass population of stars with  $m_* = 0.2 M_\odot$  or  $1 M_\odot$ . The thick lines show the capture rate assuming a more realistic Kroupa mass function which extends from  $0.2 - 1 M_\odot$ .

### 4.1 Comparison to Tidal Capture Model

For our fiducial models, we predict a total of 60–200 BH XRBs, roughly consistent with observations (Table 3). These numbers would require the luminosity function to extend a factor of  $\sim 3 - 10$  below the detection threshold. Fig. 13 shows that cumulative radial distribution of XRBs from our models at radii  $\gtrsim 0.2 \text{ pc}$  also agrees well with the distribution measured by Hailey et al. (2018).<sup>12</sup> Specifically, we predict average XRB surface density profiles  $\Sigma \propto r^{-1.4}$  and  $\propto r^{-0.9}$  in our Fiducial and Fiducial  $\times 10$  models, respectively. These slopes are consistent with the measured surface density profile of high S/N sources, which Hailey et al. (2018) find obey  $\Sigma \propto r^{-1.5 \pm 0.3}$  in the radial range  $0.2 \text{ pc} \lesssim r \lesssim 1 \text{ pc}$ .

### 4.2 Neutron Stars

The number of NS-XRBs formed in the central parsec for our Fiducial and Fiducial  $\times 10$  models are  $N_{\text{ns}} \approx 30$  and  $\approx 70$ , respectively. These numbers, which are a factor of  $\approx 2 - 3$  times lower than the predicted number of tidal capture BH-XRBs in this region, and significantly exceeds the  $\leq 3$  NS-XRBs observed thus far.

What might suppress the NS population? First, as in the BH case, not all NS binaries manifest as luminous XRBs. Furthermore, some NS-XRBs may evolve into millisecond pulsars later in their evolution. Only 3% of the known population of MSP have properties which would make them detectable in the GC (Perez et al. 2015); given that up to six of the observed X-ray sources in the central parsec could be MSPs, as many as  $\sim 200$  MSPs could exist in this region.

<sup>12</sup> We only consider those binaries outside of  $0.2 \text{ pc}$ , as observational limits prevent the identification of individual sources inside this radius.

**Table 3.** Number of tidally-captured BH- and NS-XRBs in the GC predicted for our fiducial scenarios as compared to the observed population. We only consider binaries residing in our model at radii  $\geq 0.2$  pc because observational limitations prevent source identification interior to that point. There are no strong detections ( $> 100$  counts) outside of the central parsec, but there are an additional  $\sim 40$  non-thermal sources with  $> 50$  counts between 1 and 3.5 pc (though some of these may be due to background contamination). The “Observed” XRBs corresponds to the population detected by [Hailey et al. \(2018\)](#), while the “Extrapolated” sources account for an (uncertain) extrapolation of the X-ray luminosity function below the *Chandra* detection threshold (see text for details). There are up to six MSPs among the non-thermal sources in [Hailey et al. \(2018\)](#), and as argued ([Perez et al. 2015](#)) only 3% of the MSPs in the GC would be observable. Hence there are up to 200 in the central parsec. All radii are projected.

Scenario	BH-XRB ( $r \leq 1$ pc)	BH-XRB ( $r \leq 3.5$ pc)	NS-XRB ( $r \leq 1$ pc)	NS-XRB ( $r \leq 3.5$ pc)
Fiducial	64	110	29	110
Fiducialx10	210	640	67	370
Observed	6–12	$\lesssim 50$	1–3 (LMXB), $\leq 6$ (MSP)	3–6 (LMXBs), $\lesssim 50$ (MSP)
Extrapolated	300–1000		$\lesssim 200$ (MSP)	$\lesssim 1000$ (MSP)

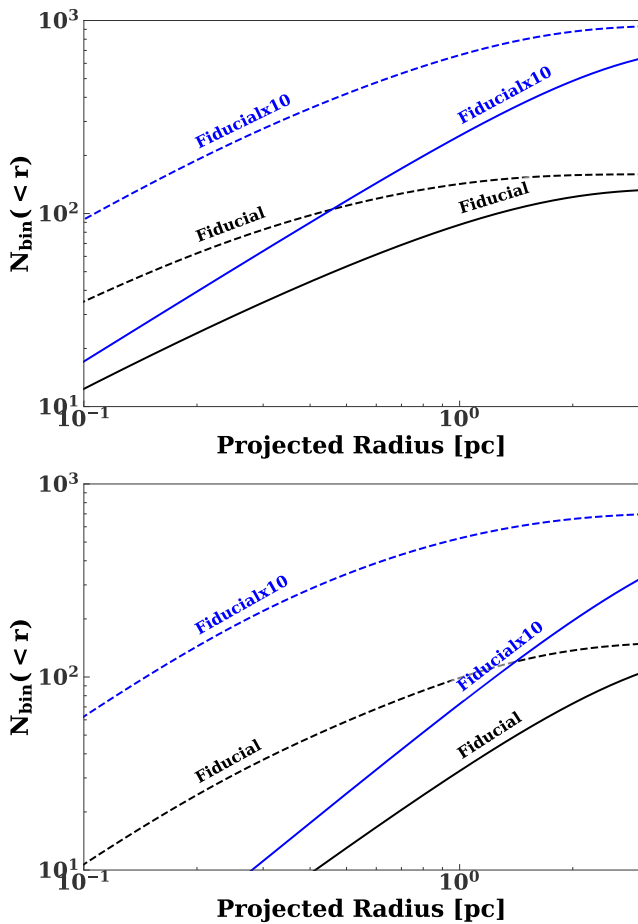


**Figure 12.** Cumulative number of tidal capture BH-XRB (top panel) and NS-XRB (bottom panel) predicted inside Galactocentric radius  $r$  for our Fiducial and Fiducial $\times 10$  scenarios. Dashed lines show the distribution of initially-formed binaries, while solid lines show the final distribution after allowing for dynamical relaxation of the binary population (these are calculated by inserting a tracer population with formed distribution of the binaries into the model snapshot corresponding the mean binary age).

The relative number of tidally captured BHs versus NSs binaries also depends on the fate of massive stars. Although we have assumed that stars of ZAMS mass  $\gtrsim 25M_{\odot}$  become BHs, in reality there is not a single mass separating BH and NS progenitors ([Sukhbold et al. 2016](#)), and the fraction of O/B stars that evolve into NSs (as opposed to BHs) may differ between the field and the GC.

The NS population could also be reduced by supernova kicks, which would eject  $\sim 40\%$  of isolated NS formed in the central disk for a Maxwellian kick velocity distribution, with  $\sigma = 265 \text{ km s}^{-1}$  ([Hobbs et al. 2005](#)). However,  $\sim 40\%$  ( $10\%$ ) of the NS binaries in our Fiducial (Fiducial $\times 10$ ) model come from NSs associated with the old stellar population, calibrated to the [Ivanova et al. \(2008\)](#) model of globular clusters (and this already accounts for supernova kicks). Overall supernova kicks would reduce the number of neutron star binaries by  $\sim 25\%$  ( $\sim 40\%$ ) in our Fiducial (Fiducial $\times 10$ ) model.

## 5 PREDICTIONS AND IMPLICATIONS OF OUR MODELS

In this section we summarize various implications of our models, including properties of binaries and rates of various electromagnetic transients (including tidal disruption events and stellar collisions). We also estimate the formation rate of BH-BH binaries due to bound-free gravitational wave emission. Table 4 summarizes the rates of these processes in our GC models.

### 5.1 Properties of binaries

XRBs formed by tidal capture are necessarily short period systems. The binaries in our models have main sequence companions with periods of  $\lesssim 10$  hours (with a median period of  $\sim 3.6$  hours). Any future periodicity identified in the quiescent population would be a powerful discriminant between tidal capture and other channels (e.g. binary exchange) that can form long period XRBs.

In the field such short-period XRBs possess low luminosities of  $\lesssim 10^{31} \text{ erg s}^{-1}$  ([Armas Padilla et al. 2014](#)) which are below the detection threshold of [Hailey et al. \(2018\)](#) and

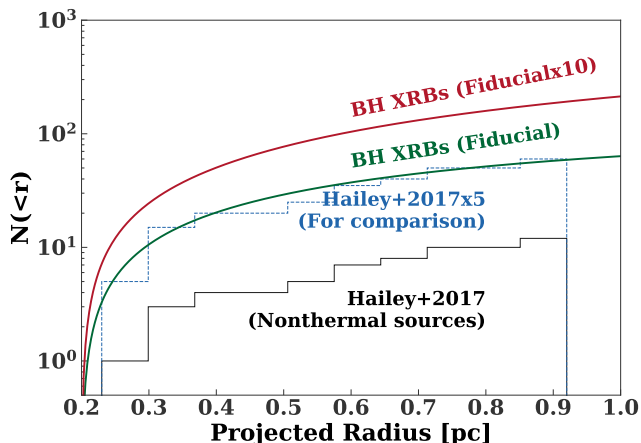


**Figure 13.** Cumulative number of BH XRBs inside projected Galactocentric radius  $r$  from our fiducial models compared with the non-thermal sources identified by Hailey et al. (2018) (black line). We have included the six sources that may be MSPs instead of BH-XRBs in the latter. The dashed blue line shows the distribution of sources scaled up to match the normalization of the Fiducial model. The region inside of 0.2 pc is not included as the population of non-thermal sources is not observationally constrained there.

thus could not be contributing to the observed population. However, the current sample of short period BH-XRBs is small (only four are known with a period of less than six hours).

## 5.2 Tidal disruptions by the central SMBH

Stars may also be tidally disrupted by the central SMBH (Hills 1975). Such tidal disruption events (TDEs) can produce bright electromagnetic flares (Rees 1988). Many candidate flares have now been detected in optical/UV (Gezari et al. 2006, 2008; van Velzen et al. 2011; Gezari et al. 2012; Chornock et al. 2014; Holoiën et al. 2014; Arcavi et al. 2014; Vinkó et al. 2015; Holoiën et al. 2016a,b; Blagorodnova et al. 2017), and X-ray wavelengths (see Auchetti et al. 2017 and the references therein).

The total TDE rate due to two-body relaxation has been estimated for a large *Hubble Space Telescope* (*HST*) samples of nearby galactic nuclei (Wang & Merritt 2004; Stone & Metzger 2016). These authors find that the average per-galaxy disruption rate is  $\sim 1 - 10 \times 10^{-4}$  per year. This range appears discrepant with observationally inferred TDE rate estimates, which are often  $\sim 10^{-5}$  galaxy $^{-1}$  yr $^{-1}$  (Donley et al. 2002; van Velzen & Farrar 2014). While recent work has suggested that properly accounting for the broad TDE luminosity function (van Velzen 2017) may bring observational TDE rates into agreement with theory, it is worth considering one limitation of the theoretical estimates: in the smallest galaxies, even *HST* observations underresolve the SMBH influence radius (from which most TDEs are sourced), and moderate inward extrapolation is needed to calibrate theoretical models (Stone & Metzger 2016). The TDE rates predicted by our Fokker-Planck models have been calibrated off scales far smaller than the Sgr A\* influence

radius, and are thus a useful sanity check on TDE rate calculations in general.

Fig. 14 shows the TDE rate for a few different models for the GC. The present-day TDE rate in each is  $\sim 10^{-4}$  stars per year ( $3 \times 10^{-5} M_{\odot}$  yr $^{-1}$ ), similar to previous theoretical estimates for SMBHs of similar size (Wang & Merritt 2004; Stone & Metzger 2016). Unsurprisingly, the *present-day* disruption rate is similar for different models as they are all tuned to reproduce the present-day observed stellar density profile. However, different star formation histories lead to very different temporal behavior in TDE rates (see also Aharon et al. 2016). In our models of the GC (Fiducial and Fiducial $\times 10$ ), all of the lower main sequence stars formed impulsively in the distant past, and the star cluster expands over time. Therefore, the TDE rate decreases at late times. In contrast, the TDE rate monotonically increases in a galactic nucleus which is continuously forming stars (see the dashed grey line in Fig. 14).

Our current sample of (thermal) TDEs is limited to the low-redshift universe, but *LSST* and *eROSITA* are expected to find TDEs out to  $z \approx 1$ . The rates of high- $z$  tidal disruption that these surveys find will therefore carry information on the growth history of nuclear star clusters (Aharon et al. 2016).<sup>13</sup>

The SMBH can accumulate a substantial fraction of its mass by disrupting stars and accreting compact objects. After a TDE half of the disrupted star is bound to the SMBH. If the SMBH consumed half of each disrupted star it would grow by  $10^6$  ( $1.6 \times 10^6$ )  $M_{\odot}$  ( $\sim 25 - 40\%$  of its present day mass). However, a significant fraction of the initially bound debris may be lost in outflows, so the mass accreted in a TDE may be  $\lesssim 10\%$  of the disrupted star’s mass (Metzger & Stone 2016). If the SMBH accretes ten percent of each disrupted star it would grow by  $3 \times 10^5$  ( $9 \times 10^5$ )  $M_{\odot}$ . For simplicity, we fix the mass of the SMBH to  $4 \times 10^6 M_{\odot}$  in our fiducial models.

## 5.3 Tidal disruptions by stellar mass compact objects

Stars that enter the tidal radius of a stellar compact object are also tidally disrupted, powering a transient flare of electromagnetic emission. We calculate the total rate of such “micro-TDEs” in our Fiducial model to be  $\sim 3 \times 10^{-7}$  per year (see Fig. 7). Thus, the micro-TDE rate in the GC is comparable to the rate from globular clusters, perturbations of wide binaries in the field, and disruptions induced by natal kicks (Perets et al. 2016). Because the resulting flare is short-lived (Perets et al. 2016 estimate the the viscous time-scale of the debris to be less than a day), it is highly unlikely any such disruption events would be observable in our own GC today. However, such events in other galactic nuclei might produce rare short-lived transients detectable at cosmological distances - for example, “ultra long” gamma ray bursts (GRBs; Levan et al. 2014). Taking into account selection effects, the total rate ultra-long GRBs may be comparable to the rate of classic long GRBs:  $\sim 10^{-6}$  per galaxy per year (at  $z = 0$ ) after beaming corrections (Guetta et al.

<sup>13</sup> Although other factors, such as the evolution of the SMBH mass function, will also contribute - see e.g. Kochanek 2016).

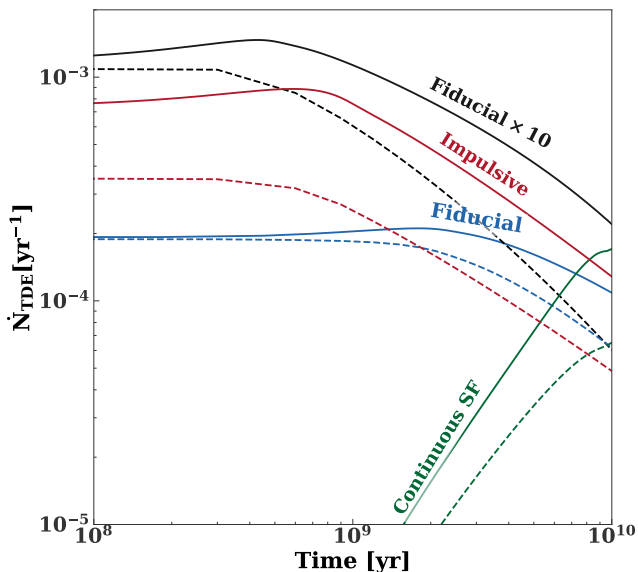


**Figure 14.** Rate of tidal disruption by the central SMBH as a function of time for our GC models (Fiducial and Fiducial $\times 10$ ). We also show hypothetical models with continuous star formation (*green line*), and a single population formed  $10^{10}$  years ago (*red lines*) (see § 2.5). The dashed lines show what the disruption rate would be without stellar mass BHs (calculated by excluding the compact objects from the angular momentum diffusion coefficients).

2005). Interestingly, this is comparable to the micro-TDE rate.

At very small Galactocentric radii, these micro-TDEs may occur without producing observable accretion flares. This will occur if the relative velocity  $v_\infty$  between the star and the compact object is too large for any of the tidal debris to remain bound, i.e. if  $v_\infty^2/2 > (m_c/m_\star)^{1/3} Gm_\star/r_\star$  (Hayasaki et al. in prep). We have excluded such hyperbolic micro-TDEs from our rate estimates.

The small mass ratio between NSs and main sequence stars means that many “micro-TDEs” involving NSs will actually be direct physical collisions, where a Thorne-Zytkow object may be formed (although the stability of such objects remains uncertain).

#### 5.4 Red giant depletion

As pointed out by Genzel et al. (1996), there is a dearth of bright red giants ( $K < 10.5$ ) within  $\sim 0.2$  pc of the GC. There is a similar dearth of intermediate luminosity ( $10.5 < K < 12$ ) giants within  $\sim 0.08$  pc. The distribution of fainter stars, on the other hand, is smooth, and has no holes on small scales.

It has been suggested that collisions of red giants with main sequence stars and BHs (Dale et al. 2009, D09 hereafter) could cause the observed holes in the red giant population. D09 find that stripping is only effective in reducing the brightness of giants in the RGB phase (and has little effect on AGB and horizontal branch stars). Furthermore, only close pericenters ( $r_p \lesssim 15R_\odot$  for a solar type giant) will remove enough material to significantly alter the evolu-

tion of the giant (see also Leigh et al. 2016). They conclude that  $2 \times 10^4$  BHs inside of 0.1 pc are required to explain the observed dearth of intermediate luminosity giants. The gap in the bright giants is harder to explain, as it would require even larger numbers of BHs that would create too large a gap in the intermediate luminosity giants.

In our Fiducial (Fiducial $\times 10$ ) model the number of BHs inside 0.1 pc is 1200 (3600), much smaller than the number required to explain the depleted giants. The intermediate luminosity giants are  $\sim 2$ -3 solar mass stars that spend  $\lesssim 100$  Myr on the giant branch. The time-scale for close encounters only becomes comparable to the giant lifetime inside of  $\sim 0.01$  pc. We conclude that it is difficult to account for the depletion of red giants by collisions with BHs alone. However, there are many alternative explanations for the dearth of red giants in the literature. For example, red giants may be destroyed by collision with a clumpy gas disk (Amaro-Seoane & Chen 2014; Kieffer & Bogdanović 2016).

Ordinary stars may also collide with each other. We calculate the present-day rate of star-star collisions outside of 0.1 pc to be  $7 \times 10^{-6}$  per year.

#### 5.5 Two body BH-BH binary formation

Close encounters between BHs can result in the formation of close binaries, either via three-body interactions or two-body gravitational wave bound-free emission (Antonini & Rasio 2016). GW capture is generally sub-dominant to three-body processes, but it is one of the few ways to produce LIGO sources with a non-negligible eccentricity. All else being equal, eccentric sources are louder and would be detectable to larger distances. Additionally, eccentric sources can sometimes provide more stringent tests of strong field gravity, as a larger fraction of the energy is emitted when the source is moving at high velocities (Loutrel et al. 2014). The maximum impact parameter that results in binary formation is

$$b_{\text{gw}} = \left( \frac{340\pi}{3} \right)^{1/7} \frac{Gm_{\text{tot}}}{c^2} \eta^{1/7} \left( \frac{v_\infty}{c} \right)^{-9/7}$$

$$\eta = \frac{m_1 m_2}{(m_1 + m_2)^2}, \quad (29)$$

as in equation 17 of O’Leary et al. (2009). The total rate of GW captures in our Fiducial (Fiducial $\times 10$ ) model is  $4 \times 10^{-11} \text{ yr}^{-1}$  ( $3 \times 10^{-10} \text{ yr}^{-1}$ ; see also Table 4), similar to lower end rate estimates in (O’Leary et al. 2009).

An estimate of the total rate of double compact object binary formation, including three-body processes, is beyond the scope of this paper, and we leave this to future work.

## 6 SUMMARY AND CONCLUSIONS

Hailey et al. (2018) have recently identified 6-12 quiescent BH-LMXB candidates within one parsec of the Galactic Center, and infer that there may be hundreds of fainter systems in the same region. This means that the GC is three orders of magnitude more efficient than the field at producing BH-XRBs, recalling the analogous massive overproduction of NS-XRBs in a different dense environment (globular clusters). While suggestive, this analogy is incomplete: NS-XRBs are dynamically manufactured in globulars by exchange interactions (e.g. binary-single scatterings), but this



**Table 4.** Present-day rates of various “exotic” collisional stellar interactions in our GC models. From top to bottom: physical collisions between ordinary stars, close encounters between BHs and red giants that would remove a significant fraction of the latter’s envelope ( $r_p \lesssim 15R_\odot$ ), disruptions of ordinary stars by the central SMBH and by smaller mass remnants, BH-BH binary formation by bound-free gravitational wave emission, ejection of stars from the GC in strong scatterings with BHs.

Interaction	Fiducial	Fiducial $\times 10$
Star-star collisions [ $\text{yr}^{-1}$ ]	$7 \times 10^{-6}$	$7 \times 10^{-6}$
BH-Red giant collisions [ $\text{yr}^{-1}$ giant $^{-1}$ at 0.1 pc]	$5 \times 10^{-11}$	$1.5 \times 10^{-10}$
micro-TDEs (BH) [ $\text{yr}^{-1}$ ]	$3 \times 10^{-7}$	$10^{-6}$
micro-TDEs (NS) [ $\text{yr}^{-1}$ ]	$6 \times 10^{-8}$	$2 \times 10^{-7}$
TDEs (SMBH) [ $\text{yr}^{-1}$ ]	$10^{-4}$	$2 \times 10^{-4}$
GW bound-free captures (BH-BH) [ $\text{yr}^{-1}$ ]	$4 \times 10^{-11}$	$3 \times 10^{-10}$
Ejection of stars by strong scattering [ $\text{yr}^{-1}$ ]	$3 \times 10^{-4}$	$10^{-3}$

mechanism is disfavored in the GC’s high velocity dispersion environment, which only permits the survival of the hardest main sequence binaries.

We instead propose that the observed LMXBs are formed via tidal capture of low mass stars by BHs. We estimated the distribution of stars and compact remnants in the GC using time-dependent Fokker-Planck models that predict close encounter rates. Taken at face value, tidal capture can explain the observed (and extrapolated) inventory of BH-XRBs in the GC. Our primary results are summarized as follows:

(i) We calculated the rate at which low mass stars are tidally captured by BHs and NS as a function of time, and used this to predict that there should be  $\sim 60$ -200 accreting BH-XRBs in the central parsec today. The number and radial distribution of these binaries is consistent with the quiescent BH-XRB population identified by Hailey et al. (2018), given reasonable extrapolation below the *Chandra* detection threshold.

(ii) Our models also produced a substantial number of NS-XRBs (far more than are currently observed). However, there are several candidate mechanisms for suppressing our predicted NS-XRB population. Alternatively, evolved NS binaries may also manifest as MSPs, whose population is poorly constrained in the GC.

(iii) The compact object source terms in our Fokker-Planck models were calibrated from the observed number of massive stars in the GC. Most of the stellar mass BHs in the GC may originate in star forming disks with a top heavy IMF, like the one currently observed at  $\sim 10^{18}$  cm (Krabbe et al. 1995; Paumard et al. 2006; Bartko et al. 2010; Lu et al. 2013). In our models, *in situ* star formation in these disks has left between  $10^4$  and  $4 \times 10^4$  BHs within the central parsec, at  $z = 0$ . Much smaller numbers of BHs would fail to explain the observed BH-XRB population, yielding the first quantitative constraints on the long-theorized “dark cusp” in the GC.

(iv) We also estimated the rates of other exotic dynamical interactions between stars and compact objects. For example, we found that the rate of disruption of stars by stellar mass BHs (“micro-tidal disruption”) in the Galactic Center is  $\sim 10^{-6}$  per year—comparable to previous estimates of the total rate in the field and globular clusters (Perets et al. 2016), as well as the rate of ultra-long GRBs (Levan

et al. 2014). The present-day TDE rate from Sgr A\* is  $\sim 1 - 3 \times 10^{-4} \text{ yr}^{-1}$ , similar to other SMBHs of its mass.

The largest theoretical uncertainty in our model is the assumption that main sequence stars tidally captured by stellar mass BHs are able to circularize and settle into stable Roche-lobe overflow. Such an outcome is not energetically guaranteed, and it is likely that BHs above a certain mass will rapidly destroy tidally captured stars by thermalizing too much mode energy inside them, leading to super-Eddington accretion in a string of partial tidal disruptions. The precise BH mass threshold above which tidal capture becomes catastrophic is an open question that we hope to address in future work. A second concern is that tidal capture binaries have periods  $\lesssim 10$  hours. In the field, such systems have low X-ray luminosities, and, if placed in the GC, would fall below the *Chandra* detection threshold. However, short period field XRBs likely have a different formation mechanism, and it is not clear if tidal capture XRBs would inherit their luminosity function.

While we have focused on tidal capture in an isotropized population of stars and compact objects, it may be fruitful to examine tidal capture within star forming disks. Though such disks are short-lived compared to the total age of the NSC, the higher densities in the disk midplane - and lower relative velocities between the stars in such a configuration - would substantially enhance the rate of tidal captures in this environment. It is also possible that stellar mass objects migrating within a gaseous disk may smoothly capture into binaries due to gas dissipation alone, even in the absence of strong tidal coupling. Finally, star-BH interactions in the MW’s most recent nuclear star forming disk might also have produced BH-HMXBs. Hailey et al. (2018) argue for a BH-LMXB interpretation due to the lack of visible optical companions, but deeper optical observations will help to further constrain this alternative.

Our tidal capture model was motivated by surprising discoveries in the MW Center, but it carries major implications for extragalactic NSCs as well. If the GC’s inventory of XRBs is representative, it may complicate X-ray searches for low-luminosity intermediate mass black hole AGN in dwarf galaxies. The unresolved, integrated X-ray luminosity from a large XRB population represents a durable if dim contaminant; a single BH-XRB in outburst would represent a more dangerous contaminant for single-epoch searches. The existence of dark cusps in galactic nuclei also carries major

implications for the highly uncertain rates of extreme mass ratio inspirals, one of the primary scientific targets for future space-based GW laser interferometers (e.g. *eLISA*). Future dynamical modeling of XRB formation in the GC may yield more sophisticated constraints on the radial profile of our dark cusp, a local laboratory with which we may calibrate our expectations for stellar dynamics in distant galactic nuclei.

#### ACKNOWLEDGMENTS

We are happy to acknowledge useful discussions with Fabio Antonini, Josh Grindlay, Nathan Leigh, Nevin Weinberg, Doug Lin, Eugene Vasiliev, Jessica Lu and Jules Halpern. We are especially grateful to Charles Hailey for discussions of his recent observational findings. NCS received financial support from NASA through Einstein Postdoctoral Fellowship Award Number PF5-160145, and thanks the Aspen Center for Physics for its hospitality during the completion of this work. BDM and AG acknowledge support from NSF Astronomy and Astrophysics grants AST-1410950, AST-1615084; NASA Astrophysics Theory Program grants NNX16AB30G, NNX17AK43G; and Hubble Space Telescope Grant HST-GO-14785.004-A.

## APPENDIX A: TIDAL COUPLING CONSTANTS

The energy deposited into a star of mass  $m_*$  after a close encounter with a compact object of mass  $m_c$  is given by

$$\Delta E = \frac{Gm_*^2}{r_*} \left(\frac{m_c}{m_*}\right)^2 \sum_{l=2}^{\infty} T_l(\eta) \left(\frac{r_*}{r_p}\right)^{(2l+2)}$$

$$\eta \equiv \left(\frac{m_*}{m_* + m_c}\right)^{1/2} \left(\frac{r_*}{r_p}\right)^{-3/2}, \quad (\text{A1})$$

where  $r_p$  is the pericenter distance of the encounter,  $r_*$  is the radius of the star, and  $T_l$  is the tidal coupling constant of multipole order  $l$ , which depends on the stellar structure and orbit.

For fixed stellar structure, the tidal coupling constant is a function of the ratio  $\eta$  of the star's dynamical time to the time spent near pericenter. For the dominant  $l = 2$  modes the energy deposited in the star is

$$\Delta E = T_2(\eta) \left(\frac{r_p}{r_t}\right)^{-6} \frac{Gm_*^2}{r_*}, \quad (\text{A2})$$

where  $r_t = r_*(m_c/m_*)^{1/3}$  is the tidal radius.

Fig. A1 compares the  $l = 2$  tidal coupling constants for both polytropic and MESA stellar models (Paxton et al. 2011, 2013).<sup>14</sup> Calculating the tidal coupling constant requires a summation over discrete stellar eigenmodes, which we calculate with GYRE (Townsend & Teitler 2013).<sup>15</sup> Following Lee & Ostriker (1986), we include the f-mode, the five lowest order p-modes, and the eighteen lowest order g-modes (if they exist) in the summation.

For stars of mass  $\lesssim 0.3 M_\odot$ , g-modes are not excited at all and most of the energy is deposited into the f-mode. Larger stellar masses and larger values of  $r_p$  result in greater energy transfer into g-modes, while p-modes are always subdominant. Fig. A2 shows the fraction of energy placed into different modes as a function of pericenter for  $m_* = 0.3 M_\odot$  and  $m_* = 1 M_\odot$  stars. An  $n = 3/2$  polytropic model accurately reproduces the mode spectrum of the low mass star. However, the mode spectrum of the solar type star is poorly approximated by a polytropic model: the  $n = 3$  polytropic model underestimates the energy in g-modes, and overestimates that in the f-mode, for small pericenter distances.

The tidal coupling constant of low mass stars ( $m_* \lesssim 0.5 M_\odot$ ), is close to that of an  $n = 3/2$  polytrope. The tidal coupling constant approaches that of an  $n = 3$  polytrope as the stellar mass approaches  $1 M_\odot$ .

## APPENDIX B: CORRECTIONS FOR NON-LINEAR EFFECTS

Linear theory underestimates the energy deposited in the star by a factor of a few for the close pericenters of interest. Non-linear corrections have been calculated by Ivanov & Novikov (2001) for polytropic stellar models. We adopt their prescriptions for the tidal coupling constant for close pericenters.

<sup>14</sup> <http://mesa.sourceforge.net>, version 9575

<sup>15</sup> <https://bitbucket.org/rhdtownsend/gyre/wiki/Home>, version 5. We assume adiabatic oscillations.

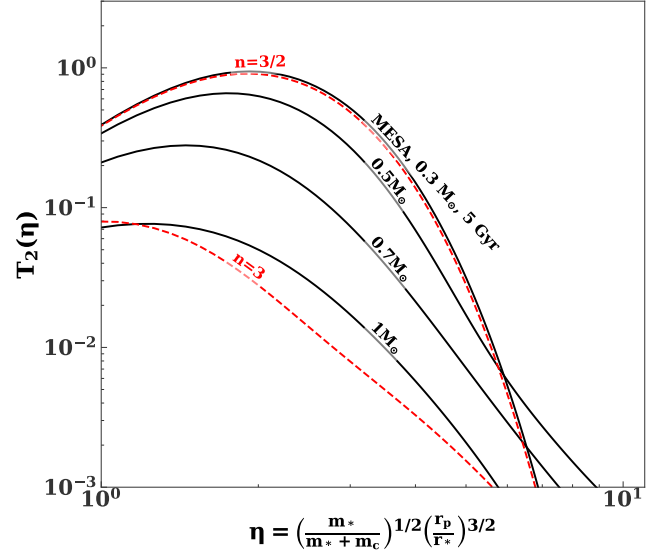


**Figure A1.** Comparison of tidal coupling constant as a function of  $\eta$  (eq. A1) for different stellar models as labeled. The dashed, red lines show the tidal coupling constants for polytropic stellar models. We have assumed a parabolic orbit.

Fig. B1 compares tidal coupling constants for polytropic models from linear theory and from Ivanov & Novikov (2001) (see also their Figures 13 and 15). The following expressions reproduce tidal coupling constants from Ivanov & Novikov (2001) for small pericenters, while approaching the results of linear theory at large pericenters.

$n=3/2$  polytrope:

$$T(\eta) = C 2^{(b-g)/s} \left(\frac{\eta}{\eta_o}\right)^{-g} \left(1 + \left(\frac{\eta}{\eta_o}\right)^s\right)^{(g-b)/s}$$

$$\times \left(\frac{1}{2} - \frac{1}{2} \tanh \left[ k \left(\frac{r}{r_1} - 1\right) \right]\right)$$

$$C = 2.58, \eta_o = 1.73, g = -4.36, b = 2.82, s = 9.91,$$

$$r_1 = 4.5, k = 4 \quad (\text{B1})$$

$n=3$  polytrope:

$$T(\eta) = C 2^{(b-g)/s} \left(\frac{\eta}{\eta_o}\right)^{-g} \left(1 + \left(\frac{\eta}{\eta_o}\right)^s\right)^{(g-b)/s}$$

$$\times \left(1 + \left(\frac{\eta}{\eta_1}\right)^{s_2}\right)^{(b-b_2)/s_2}$$

$$C = 0.17, \eta_o = 1.07, \eta_1 = 1.92, g = -3.83,$$

$$b = 5.5, b_2 = 3.49, s = 3.59, s_2 = 6.68, \quad (\text{B2})$$

where we have adopted eq. (B1) for low mass stars with  $m_* \leq 0.7 M_\odot$ , and eq. (B2) for higher stellar masses.

## APPENDIX C: BINARY EXCHANGE INTERACTIONS

### C1 Binary fraction

When *soft* binaries interact with field stars in the GC they gain energy, become more loosely bound, and eventually dissociate (Heggie 1975; Binney & Tremaine 1987). A binary

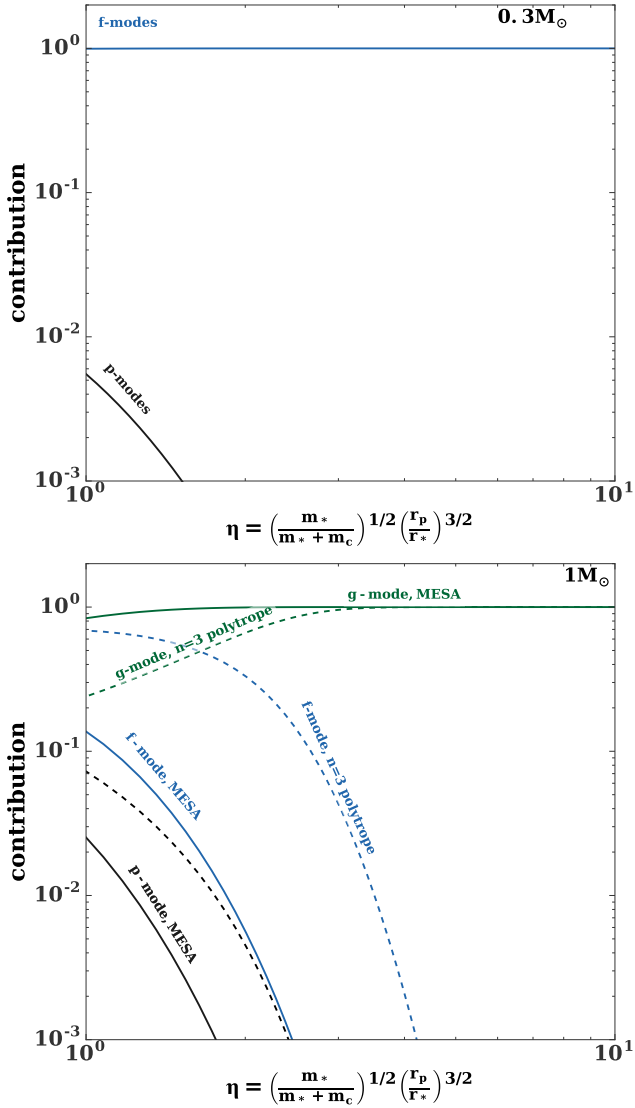


**Figure A2.** *Top panel:* Fraction of oscillation energy deposited into p-, f-, and g-modes for a star of mass  $0.3 M_{\odot}$ . For this calculation we use a MESA model evolved for 5 Gyr, but the results are indistinguishable from that of an  $n = 3/2$  polytrope. The g-modes do not contribute. *Bottom panel:* Same as the top panel, but for a star of mass  $1 M_{\odot}$ . The mode decomposition is not accurately reproduced by a polytropic model, as can be seen by comparing the solid and dashed lines.

is soft if its binding energy is less than the kinetic energy of a typical field star, i.e. if,

$$\frac{Gm_1m_2}{a\langle m \rangle} < \sigma^2, \quad (\text{C1})$$

where  $m_1$  and  $m_2$  are the masses of the binary components,  $a$  is the semi-major axis,  $\langle m \rangle$  is the mean stellar mass, and  $\sigma$  is the 1D velocity dispersion. Binaries that do not satisfy eq. (C1) are *hard*. Interactions with field stars shrink the separation of a hard binary over time, making it a smaller target. Thus, it is much easier (and faster) to dissolve a soft binary than to push a hard binary to coalescence.

The black lines in Fig. C1 shows the hard-soft boundary

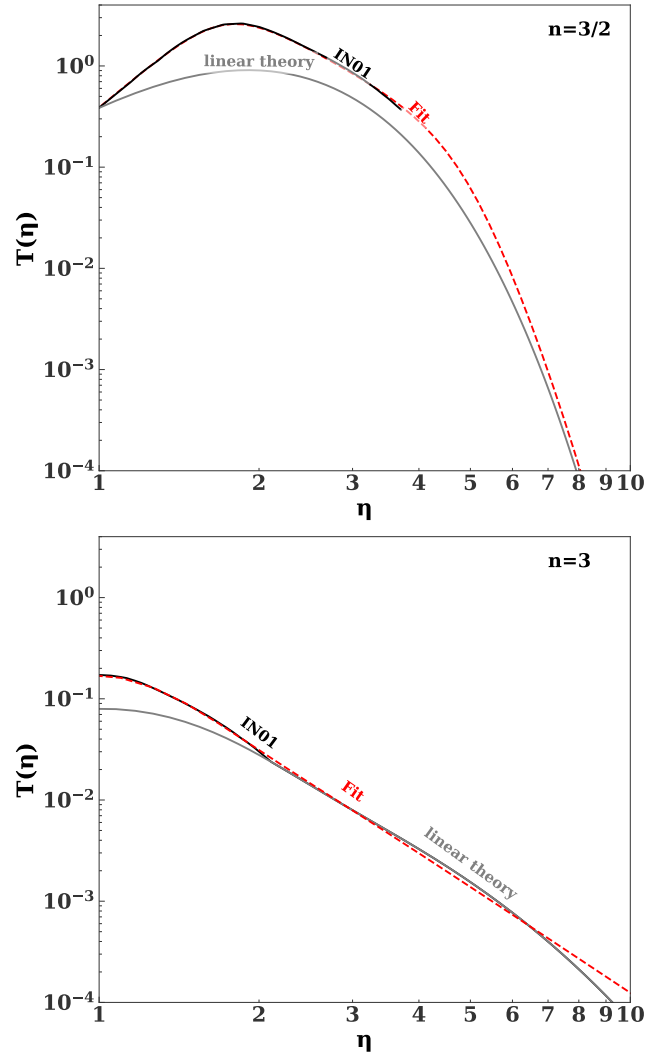


**Figure B1.** Fitted tidal coupling constants  $T(\eta)$  from the non-linear results of Ivanov & Novikov (2001). Results are shown for  $n = 3/2$  (top panel) and  $n = 3$  (bottom panel) polytropes.

in our Fiducial model of the Galactic Center for two different binary masses. For a binary distribution that is flat in  $\log(a)$ , from the semi-major axis of Roche-Lobe contact  $a_{\text{roche}} \approx r_t \sim R_*$  to  $a = 900$  AU, we find that  $\sim 73\%$  (87%) of binaries with two solar mass ( $0.3$  solar mass stars) are soft at 1 pc. By contrast, in a globular cluster with  $\sigma \sim 10$  km s $^{-1}$ , only 40–50% of the primordial binaries are soft (Ivanova et al. 2005).

Soft binaries can be ionized in two different ways:

a Direct collisions with field stars, as occurs on a timescale

$$t_{\text{collide}} = \frac{1}{\pi n_* \sigma a^2 \left(1 + \frac{2G(m_1+m_2)}{\sigma^2 a}\right)}. \quad (\text{C2})$$

In our fiducial models, the collision rate of binaries with stars exceeds the collision rate of binaries with compact objects.

b “Evaporation” due to perturbations from distant field

stars. For an equal mass binary this occurs on a timescale (Alexander & Pfuhl 2014; their eq. 3)

$$t_{\text{evap}} \approx 0.07 \frac{(m_1 + m_2)\sigma}{Gn\langle m^2 \rangle \ln \Lambda}, \quad (\text{C3})$$

where  $m_{\text{bin}}$  is the total mass of the binary,  $n$  is the number density of perturbers,  $\langle m^2 \rangle$  is the second moment of the mass function,  $\sigma$  is the 1D velocity dispersion, and  $\ln \Lambda \approx 15$  is the Coulomb logarithm.

The red lines in Fig. C1 show the semi-major axes for which the collision and evaporation times are equal to  $10^{10}$  years. Any primordial binaries with semi-major axes  $\gtrsim 0.1$  AU within the central parsec would be evaporated on a timescale of  $\lesssim 10^{10}$  yr.

On the other hand, binaries with particularly *small* semi-major axes can be destroyed by magnetic braking. Following Ivanova & Kalogera (2006) (their eq. 4), we find that two stars of mass  $m_*$  with semi-major axes obeying

$$a < 3 \left( \frac{m_*}{M_\odot} \right)^{0.16} \left( \frac{t}{10 \text{ Gyr}} \right)^{0.41} a_{\text{roche}}, \quad (\text{C4})$$

are brought into Roche-Lobe contact after time  $t$ . Solar mass stars in a two day orbit would thus come into Roche-Lobe contact within  $\lesssim 5$  Gyr (see also Andronov et al. 2006).

The binary fraction is

$$f_b \equiv \frac{N_b}{N_s + N_b} = \frac{(1 - f_d)f_{b,0}}{1 + f_d f_{b,0}} \quad (\text{C5})$$

where  $N_b$  and  $N_s$  are the numbers of single stars and binaries respectively,  $f_{b,0}$  is the initial binary fraction and  $f_d$  is the fraction that are destroyed due to the effects of evaporation and/or magnetic braking. Figure C2 shows the expected binary fraction at 1 pc after 5 and 10 Gyr, as a function of stellar mass (assuming equal mass binaries). Weighting each mass bin by a Kroupa PDMF, we find that the binary fraction is  $\sim 4\%$  ( $3\%$ ) after 5 (10) Gyr. Our estimate for the binary fraction of solar mass stars accounting evaporation alone ( $\sim 10\%$ ) is comparable to previous estimates (Hopman 2009).

Kozai-Lidov (KL) oscillations induced by the central SMBH can turn some soft binaries into hard binaries, effectively increasing the binary fraction. In particular, KL oscillations can excite binaries to very large eccentricities. Tides can then dissipate energy, creating a tight stellar binary (Antonini & Perets 2012; Stephan et al. 2016). In practice, for the Galactocentric radii of interest ( $\sim 1$  pc), the time-scale to excite the binary to very large eccentricities (the *octupole* Kozai time scale) is generally longer than the evaporation time-scale. Additionally, for a  $1M_\odot$  binary, GR precession will damp KL oscillations for binary separations

$$a_1 < 2 \text{ au} \left( \frac{a_2}{1 \text{ pc}} \right)^{3/4} \frac{(1 - e_2^2)^{3/8}}{(1 - e_1^2)^{1/4}}, \quad (\text{C6})$$

where  $e_1$  is the eccentricity of the inner binary orbit, while  $a_2$  and  $e_2$  are the semi-major axis and eccentricity of the binary's orbit around the SMBH (see equation 59 in Naoz 2016).

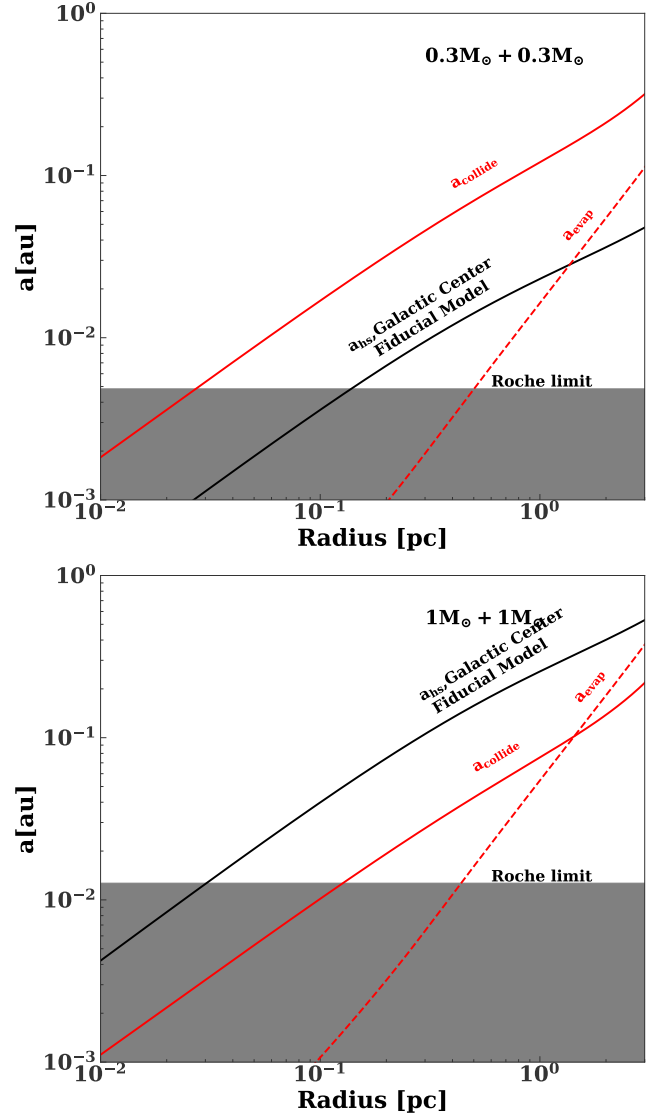


**Figure C1.** Hard-soft boundary for  $1+1 M_\odot$  (top panel) and  $0.3+0.3 M_\odot$  (bottom panel) in our fiducial model for the GC. The red lines show the semi-major axis for which the time-scale for direct collisions (eq. C2) and evaporation (eq. C3) is  $10^{10}$  years. Binaries in the gray region are either contact binaries or unphysical as the semi-major axis of the binary would be smaller than the Roche limit.

## C2 Binary exchange rates

Finally, the rate of compact objects exchanging into existing stellar binaries is

$$\dot{n}_{2+1} = \int_0^\infty n_c f_b n_* \Sigma v_\infty f(v_\infty) dv_\infty, \quad (\text{C7})$$

where  $n_c$  and  $n_*$  are the densities of compact objects (BHs or NSs) and stars, respectively, and  $\Sigma$  is the total cross-section for the compact object to be captured into a binary with an ordinary star. This may either occur via a *prompt exchange* or a *resonant capture*. In the former case the exchange occurs quickly, while in the latter case a metastable triple system is formed first. The cross-sections for these processes have been calibrated from binary-single scattering experiments as

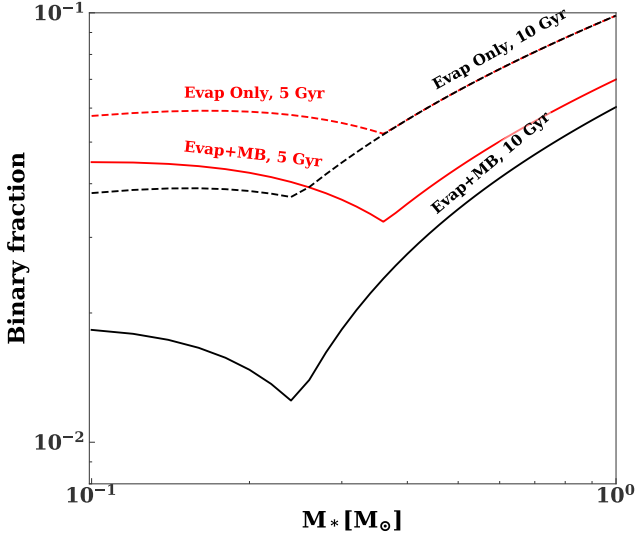


**Figure C2.** Binary fraction at 1 pc after 5 Gyr (red lines) and 10 (black lines) Gyr, calculated for an assumed initial binary fraction of 50%. For the dashed lines we only account for evaporation of soft binaries, while for the solid lines we account for the destruction of hard binaries via magnetic braking. The x-axis indicates the mass of each of the stars in the binary.

(Valtonen & Karttunen 2006)

$$\Sigma_{\text{ex}} \approx 0.51 \frac{2m_c \pi a^2}{m_* v^2} (1 - P_c) \quad (\text{C8})$$

$$\Sigma_{\text{cap}} \approx 1.18(n-1)(1-v^2)^{n-2} \frac{2m_c \pi a^2}{m_* v^2} (1 - P_s) \quad (\text{C9})$$

$$P_c \approx 0.25(n-1)(1-v^2)^{n-2} \quad (\text{C10})$$

$$P_s = \frac{m_c^{-q}}{2m_*^{-q} + m_c^{-q}} \quad (\text{C11})$$

$$v^2 = \frac{2m_c v_\infty^2 a_0}{M G m_*}, \quad (\text{C12})$$

where  $m_c$ ,  $m_*$ , and  $M$  are the masses of the compact object, the stars in the binary (assumed to be equal in mass), and the three-body system, respectively. The cross-sections go to 0 for  $v \gtrsim 1$ . The power law index  $n$  ( $q$ ) depends on the angular momentum of the system, and is expected to vary between 4.5 and 3 (1 and 3) as  $v$  goes from 0 to 1. We choose  $n = q = 3$ , but the results are not very sensitive to this choice.

Using densities profiles of our Fiducial model, the rate of 2+1 encounters per unit volume at radii  $\lesssim 1$  pc is approximately given by

$$\begin{aligned} \dot{n}_{\text{bh},2+1} &= 5 \times 10^{-11} \left( \frac{r}{1\text{pc}} \right)^{-2.5} \left( \frac{f_b}{0.01} \right) \left( \frac{m_*}{\bar{m}_*} \right) \text{pc}^{-3} \text{yr}^{-1} \\ \dot{n}_{\text{ns},2+1} &= 3 \times 10^{-11} \left( \frac{r}{1\text{pc}} \right)^{-1.9} \left( \frac{f_b}{0.01} \right) \left( \frac{m_*}{\bar{m}_*} \right) \text{pc}^{-3} \text{yr}^{-1} \end{aligned} \quad (\text{C13})$$

where  $\bar{m}_* = 0.3M_\odot$ . Integrating over volume and a Kroupa PDMF ( $m_* = 0.2 - 1M_\odot$ ), we find that the total rate of 2+1

encounters inside of 1 pc is

$$\begin{aligned} \dot{N}_{\text{bh},2+1} &= 8 \times 10^{-10} \left( \frac{f_b}{0.01} \right) \text{yr}^{-1} \\ \dot{N}_{\text{ns},2+1} &= 4 \times 10^{-10} \left( \frac{f_b}{0.01} \right) \text{yr}^{-1}, \end{aligned} \quad (\text{C14})$$

where we have truncated the volume integral where  $a_{\text{hs}}$  equals the stellar radius. Comparing to the tidal capture rates (Fig. 11), we see the rate of 2+1 encounters is sub-dominant for binary fractions of  $\lesssim 50\%$  for BHs and 15% for NSs, as expected in the GC from the above considerations. We stress that these calculations are generous to the 2+1 formation channel, as we have assumed that every exchange interaction involving a main sequence binary and a compact object will lead to XRB formation, while in reality this is only true for a subset of these interactions. For example, three-body interactions can result in a physical stellar collision (Fregeau et al. 2004). Thus, for the low binary fractions expected in the GC, binary-single exchange interactions should be highly sub-dominant to tidal capture in the formation of XRBs.

## REFERENCES

- Aharon D., Perets H. B., 2015, *ApJ*, **799**, 185  
 Aharon D., Mastrobuono Battisti A., Perets H. B., 2016, *ApJ*, **823**, 137  
 Alexander T., Hopman C., 2009, *ApJ*, **697**, 1861  
 Alexander T., Kumar P., 2001, *ApJ*, **549**, 948  
 Alexander T., Morris M., 2003, *ApJ*, **590**, L25  
 Alexander T., Pfuhl O., 2014, *ApJ*, **780**, 148  
 Amaro-Seoane P., Chen X., 2014, *ApJ*, **781**, L18  
 Andronov N., Pinsonneault M. H., Terndrup D. M., 2006, *ApJ*, **646**, 1160  
 Antonini F., Perets H. B., 2012, *ApJ*, **757**, 27  
 Antonini F., Rasio F. A., 2016, *ApJ*, **831**, 187  
 Arcavi I., et al., 2014, *ApJ*, **793**, 38  
 Armas Padilla M., Wijnands R., Degenaar N., Muñoz-Darias T., Casares J., Fender R. P., 2014, *MNRAS*, **444**, 902  
 Auchettl K., Guillochon J., Ramirez-Ruiz E., 2017, *ApJ*, **838**, 149  
 Bahcall J. N., Wolf R. A., 1976, *ApJ*, **209**, 214  
 Bahcall J. N., Wolf R. A., 1977, *ApJ*, **216**, 883  
 Bahramian A., et al., 2014, *ApJ*, **780**, 127  
 Bahramian A., et al., 2017, *MNRAS*, **467**, 2199  
 Banerjee S., Baumgardt H., Kroupa P., 2010, *MNRAS*, **402**, 371  
 Bar-Or B., Alexander T., 2016, *ApJ*, **820**, 129  
 Bartko H., et al., 2010, *ApJ*, **708**, 834  
 Bartos I., Kocsis B., Haiman Z., Márka S., 2017, *ApJ*, **835**, 165  
 Baumgardt H., Amaro-Seoane P., Schödel R., 2017, preprint, ([arXiv:1701.03818](https://arxiv.org/abs/1701.03818))  
 Benacquista M. J., Downing J. M. B., 2013, *Living Reviews in Relativity*, **16**, 4  
 Binney J., Tremaine S., 1987, *Galactic dynamics*  
 Blagorodnova N., et al., 2017, *ApJ*, **844**, 46  
 Brandt T. D., Kocsis B., 2015, *ApJ*, **812**, 15  
 Breen P. G., Heggie D. C., 2012, *MNRAS*, **425**, 2493  
 Breen P. G., Heggie D. C., 2013, *MNRAS*, **432**, 2779  
 Buchholz R. M., Schödel R., Eckart A., 2009, *A&A*, **499**, 483  
 Chornock R., et al., 2014, *ApJ*, **780**, 44  
 Cohn H., 1985, in Goodman J., Hut P., eds, *IAU Symposium Vol. 113, Dynamics of Star Clusters*. pp 161–177  
 Corral-Santana J. M., Casares J., Muñoz-Darias T., Bauer F. E., Martínez-Pais I. G., Russell D. M., 2016, *A&A*, **587**, A61  
 Dale J. E., Davies M. B., Church R. P., Freitag M., 2009, *MNRAS*, **393**, 1016

- Degenaar N., Wijnands R., Cackett E. M., Homan J., in't Zand J. J. M., Kuulkers E., Maccarone T. J., van der Klis M., 2012, *A&A*, **545**, A49
- Degenaar N., Wijnands R., Miller J. M., Reynolds M. T., Kennea J., Gehrels N., 2015, *Journal of High Energy Astrophysics*, **7**, 137
- Do T., Ghez A. M., Morris M. R., Lu J. R., Matthews K., Yelda S., Larkin J., 2009, *ApJ*, **703**, 1323
- Donley J. L., Brandt W. N., Eracleous M., Boller T., 2002, *AJ*, **124**, 1308
- Dubus G., Lasota J.-P., Hameury J.-M., Charles P., 1999, *MNRAS*, **303**, 139
- Fabian A. C., Pringle J. E., Rees M. J., 1975, *MNRAS*, **172**, 15p
- Fragione G., Sari R., 2017, preprint, ([arXiv:1712.03242](https://arxiv.org/abs/1712.03242))
- Frank J., King A., Raine D. J., 2002, *Accretion Power in Astrophysics: Third Edition*
- Fregeau J. M., Cheung P., Portegies Zwart S. F., Rasio F. A., 2004, *MNRAS*, **352**, 1
- Freitag M., Amaro-Seoane P., Kalogera V., 2006, *ApJ*, **649**, 91
- Fuller J., Lai D., 2011, *MNRAS*, **412**, 1331
- Fuller J., Lai D., 2012, *MNRAS*, **421**, 426
- Genzel R., Thatte N., Krabbe A., Kroker H., Tacconi-Garman L. E., 1996, *ApJ*, **472**, 153
- Genzel R., et al., 2003, *ApJ*, **594**, 812
- Georgiev I. Y., Böker T., 2014, *MNRAS*, **441**, 3570
- Gezari S., et al., 2006, *ApJ*, **653**, L25
- Gezari S., et al., 2008, *ApJ*, **676**, 944
- Gezari S., et al., 2012, *Nature*, **485**, 217
- Gnedin O. Y., Ostriker J. P., Tremaine S., 2014, *ApJ*, **785**, 71
- Guetta D., Piran T., Waxman E., 2005, *ApJ*, **619**, 412
- Guillochon J., Ramirez-Ruiz E., 2013, *ApJ*, **767**, 25
- Habibi M., et al., 2017, *ApJ*, **847**, 120
- Hailey C. J., Mori K., 2017, in *AAS/High Energy Astrophysics Division*. p. 109.12
- Hailey C. J., Mori K., Bauer F., Berkowitz M. E., Hong J., Hord B., 2018, Accepted to *Nature*
- Heggie D. C., 1975, *MNRAS*, **173**, 729
- Heinke C. O., Grindlay J. E., Lugger P. M., Cohn H. N., Edmonds P. D., Lloyd D. A., Cool A. M., 2003, *ApJ*, **598**, 501
- Heinke C. O., Grindlay J. E., Edmonds P. D., 2005a, *ApJ*, **622**, 556
- Heinke C. O., Grindlay J. E., Edmonds P. D., Cohn H. N., Lugger P. M., Camilo F., Bogdanov S., Freire P. C., 2005b, *ApJ*, **625**, 796
- Heinke C. O., Wijnands R., Cohn H. N., Lugger P. M., Grindlay J. E., Pooley D., Lewin W. H. G., 2006, *ApJ*, **651**, 1098
- Hénon M., 1969, *A&A*, **2**, 151
- Hills J. G., 1975, *Nature*, **254**, 295
- Hobbs G., Lorimer D. R., Lyne A. G., Kramer M., 2005, *MNRAS*, **360**, 974
- Holoien T. W.-S., et al., 2014, *MNRAS*, **445**, 3263
- Holoien T. W.-S., et al., 2016a, preprint, ([arXiv:1602.01088](https://arxiv.org/abs/1602.01088))
- Holoien T. W.-S., et al., 2016b, *MNRAS*, **455**, 2918
- Hopman C., 2009, *ApJ*, **700**, 1933
- Hopman C., Alexander T., 2006a, *ApJ*, **645**, 1152
- Hopman C., Alexander T., 2006b, *ApJ*, **645**, L133
- Hurley J. R., Pols O. R., Tout C. A., 2000, *MNRAS*, **315**, 543
- Ivanov P. B., Novikov I. D., 2001, *ApJ*, **549**, 467
- Ivanova N., Kalogera V., 2006, *ApJ*, **636**, 985
- Ivanova N., Belczynski K., Fregeau J. M., Rasio F. A., 2005, *MNRAS*, **358**, 572
- Ivanova N., Heinke C. O., Rasio F. A., Belczynski K., Fregeau J. M., 2008, *MNRAS*, **386**, 553
- Katz J. I., 1975, *Nature*, **253**, 698
- Kieffer T. F., Bogdanović T., 2016, *ApJ*, **823**, 155
- Kochanek C. S., 1992, *ApJ*, **385**, 604
- Kochanek C. S., 2016, *MNRAS*, **461**, 371
- Kocsis B., Tremaine S., 2011, *MNRAS*, **412**, 187
- Krabbe A., et al., 1995, *ApJ*, **447**, L95
- Kremer K., Chatterjee S., Rodriguez C. L., Rasio F. A., 2017, preprint, ([arXiv:1709.05444](https://arxiv.org/abs/1709.05444))
- Kulkarni S. R., Hut P., McMillan S., 1993, *Nature*, **364**, 421
- Kumar P., Goodman J., 1996, *ApJ*, **466**, 946
- Lee H. M., Ostriker J. P., 1986, *ApJ*, **310**, 176
- Leigh N. W. C., Antonini F., Stone N. C., Shara M. M., Merritt D., 2016, *MNRAS*, **463**, 1605
- Leigh N. W. C., et al., 2017, preprint, ([arXiv:1711.10494](https://arxiv.org/abs/1711.10494))
- Levan A. J., et al., 2014, *ApJ*, **781**, 13
- Levin Y., Beloborodov A. M., 2003, *ApJ*, **590**, L33
- Lin D. N. C., Tremaine S., 1980, *ApJ*, **242**, 789
- Linial I., Sari R., 2017, *MNRAS*, **469**, 2441
- Loutrel N., Yunes N., Pretorius F., 2014, *Phys. Rev. D*, **90**, 104010
- Lu J. R., Do T., Ghez A. M., Morris M. R., Yelda S., Matthews K., 2013, *ApJ*, **764**, 155
- Maccarone T. J., Kundu A., Zepf S. E., Rhode K. L., 2007, *Nature*, **445**, 183
- Mardling R. A., 1995, *ApJ*, **450**, 722
- Merritt D., 2010, *ApJ*, **718**, 739
- Merritt D., 2013, *Dynamics and Evolution of Galactic Nuclei*
- Merritt D., 2015, *ApJ*, **804**, 52
- Metzger B. D., Stone N. C., 2016, *MNRAS*, **461**, 948
- Miller-Jones J. C. A., et al., 2015, *MNRAS*, **453**, 3918
- Miralda-Escudé J., Gould A., 2000, *ApJ*, **545**, 847
- Mori K., et al., 2013, *ApJ*, **770**, L23
- Morris M., 1993, *ApJ*, **408**, 496
- Morscher M., Pattabiraman B., Rodriguez C., Rasio F. A., Umbreit S., 2015, *ApJ*, **800**, 9
- Muno M. P., Pfahl E., Baganoff F. K., Brandt W. N., Ghez A., Lu J., Morris M. R., 2005, *ApJ*, **622**, L113
- Naos S., 2016, *ARA&A*, **54**, 441
- O'Leary R. M., Kocsis B., Loeb A., 2009, *MNRAS*, **395**, 2127
- Paczynski B., Trimble V., 1979, in *Burton W. B., ed., IAU Symposium Vol. 84, The Large-Scale Characteristics of the Galaxy*. pp 401–403
- Paumard T., et al., 2006, *ApJ*, **643**, 1011
- Paxton B., Bildsten L., Dotter A., Herwig F., Lesaffre P., Timmes F., 2011, *ApJS*, **192**, 3
- Paxton B., et al., 2013, *ApJS*, **208**, 4
- Peebles P. J. E., 1972, *ApJ*, **178**, 371
- Perets H. B., Li Z., Lombardi Jr. J. C., Milcarek Jr. S. R., 2016, *ApJ*, **823**, 113
- Perez K., et al., 2015, *Nature*, **520**, 646
- Peters P. C., 1964, *Physical Review*, **136**, 1224
- Pfahl E., Loeb A., 2004, *ApJ*, **615**, 253
- Pfuhl O., et al., 2011, *ApJ*, **741**, 108
- Pooley D., Hut P., 2006, *ApJ*, **646**, L143
- Press W. H., Teukolsky S. A., 1977, *ApJ*, **213**, 183
- Quinlan G. D., Shapiro S. L., 1987, *ApJ*, **321**, 199
- Rauch K. P., Tremaine S., 1996, *New A*, **1**, 149
- Rees M. J., 1988, *Nature*, **333**, 523
- Sazonov S., Sunyaev R., Revnivtsev M., 2012, *MNRAS*, **420**, 388
- Schödel R., Gallego-Cano E., Dong H., Noguera-Lara F., Gallego-Calvente A. T., Amaro-Seoane P., Baumgardt H., 2018, *A&A*, **609**, A27
- Spitzer L., 1987, *Dynamical evolution of globular clusters*
- Stephan A. P., Naos S., Ghez A. M., Witzel G., Sitarski B. N., Do T., Kocsis B., 2016, *MNRAS*, **460**, 3494
- Stone N. C., Metzger B. D., 2016, *MNRAS*, **455**, 859
- Stone N. C., Metzger B. D., Haiman Z., 2017a, *MNRAS*, **464**, 946
- Stone N. C., Küpper A. H. W., Ostriker J. P., 2017b, *MNRAS*, **467**, 4180
- Strader J., Chomiuk L., Maccarone T. J., Miller-Jones J. C. A., Seth A. C., 2012a, *Nature*, **490**, 71
- Strader J., Chomiuk L., Maccarone T. J., Miller-Jones J. C. A., Seth A. C., Heinke C. O., Sivakoff G. R., 2012b, *ApJ*, **750**, L27

- Sukhbold T., Ertl T., Woosley S. E., Brown J. M., Janka H.-T., 2016, *ApJ*, **821**, 38
- Tetarenko B. E., et al., 2016, *ApJ*, **825**, 10
- Townsend R. H. D., Teitler S. A., 2013, *MNRAS*, **435**, 3406
- Tremaine S. D., Ostriker J. P., Spitzer Jr. L., 1975, *ApJ*, **196**, 407
- Tsang D., 2013, *ApJ*, **777**, 103
- Valtonen M., Karttunen H., 2006, *The Three-Body Problem*
- Vasiliev E., 2017, *ApJ*, **848**, 10
- Verbunt F., Hut P., 1987, in Helfand D. J., Huang J.-H., eds, *IAU Symposium Vol. 125, The Origin and Evolution of Neutron Stars*. p. 187
- Vinkó J., et al., 2015, *ApJ*, **798**, 12
- Wang J., Merritt D., 2004, *ApJ*, **600**, 149
- Wu Y., 2017, preprint, ([arXiv:1710.02542](https://arxiv.org/abs/1710.02542))
- Yungelson L. R., Lasota J.-P., Nelemans G., Dubus G., van den Heuvel E. P. J., Dewi J., Portegies Zwart S., 2006, *A&A*, **454**, 559
- van Velzen S., 2017, preprint, ([arXiv:1707.03458](https://arxiv.org/abs/1707.03458))
- van Velzen S., Farrar G. R., 2014, *ApJ*, **792**, 53
- van Velzen S., et al., 2011, *ApJ*, **741**, 73